PhD dissertation

The scattering patterns from periodic surfaces.

by

Piotr Garstecki

written under the supervision of

prof. Robert Hołyst

October 2001

Institute of Physical Chemistry PAS
Dept. III, Kasprzaka 44/52
01-224 Warsaw
Poland

Dziękuję mojemu promotorowi profesorowi Robertowi Hołystowi za wybranie tematu, stymulujące dyskusje oraz opiekę podczas realizacji projektu. Jestem również niezmiernie wdzięczny wszystkim pracownikom zakładu III.go za stworzenie przyjaznej atmosfery pracy. Szczególnie dziękuję doktorowi Marcinowi Fiałkowskiemu, którego wiedza i trafne uwagi był nieocenioną pomocą.

Dziękuję również rodzicom za wsparcie radą i obiadą.

Pracę tę dedykuję mojej żonie i Stasiowi.

Acknowledgments

The research described in this thesis has been supported
by KBN grants 2P03B12516 (1998-2000) and 5 P03B 084 21 (2001-2002).

List of publications

- 1. P. Garstecki, T. X. Hoang, M. Cieplak, "Energy Landscapes, supergraphs, and 'Folding Funnels' in spin systems" Phys. Rev. E, 60, 3, 3219 (1999)
- 2. P. Garstecki, R. Hołyst, "Scattering on Triply Periodic Minimal Surfaces - the Effect of the Topology, Debye-Waller, and Molecular Form Factors" J. Chem. Phys. 113, 9, 3772 (2000)
- 3. P. Garstecki, R. Hołyst, "Periodic surfaces of simple and complex topology: comparison of scattering patterns" Phys. Rev. E, 6402, 2, 1501 (2001)
- 4. P. Garstecki, R. Hołyst, "Szamponowy kalejdoskop" submitted to *Wiedza i Życie*
- 5. P. Garstecki, R. Hołyst, "Scattering patterns of self assembled gyroid cubic phases in amphiphilic systems" J. Chem. Phys. 115, 2, 1095 (2001)
- 6. P. Garstecki, R. Hołyst, "The scattering patterns of self-assembled cubic phases. 1. The model." accepted to *Langmuir*
- 7. P. Garstecki, R. Hołyst, "The scattering patterns of self-assembled cubic phases. 2. Analysis of the experimental spectra." accepted to *Langmuir*

Thesis

Despite the fact that the x-ray spectra of the self assembled cubic phases have been known since 1968 there are no simple theoretical tools for their analysis. The theoretical analysis have been hampered by the mathematical and structural complexity of the unit cells of the cubic structures. For one, a single cubic cell contains hundreds of thousands of complex molecules and a basic mathematical motive in a unit cell is a periodic surface of complex shape.

We will prove that the scattering amplitudes of the self assembled cubic phases in amphiphilic mixtures can be very well approximated by the following relation:

$$A(\mathrm{q}, \rho(\xi), \sigma) = F^S \left[2 \int_0^\infty d\xi \rho(\xi) \cos(q\ \alpha_{hkl}\ \xi) \right] \exp\left[-\frac{1}{2} (q\ \alpha_{hkl}\ \sigma)^2 \right]$$

where $\mathrm{q} = (2\pi/a)[h, k, l]$ is the scattering wave vector, a is the cubic cell parameter, ξ is a coordinate along the normal to the base periodic surface, $\rho(\xi)$ is a density distribution in the direction normal to the surface and σ is a parameter proportional to the fluctuations amplitude of the structure. All of the data (structure factors $F^S(\mathrm{q})$ and correction parameters α_{hkl}) needed to evaluate this expression for any density distribution and fluctuations have been determined numerically for the P, D, G, C(D), C(P), F-RD and I-WP triply periodic surface based cubic phases.

For a preliminary analysis of the experimental scattering patterns we propose a simplified model based on the assumption of an uniform density distribution with constant density ρ_0 inside the layer of width L and neglecting the fluctuations:

$$A(\mathrm{q}, L) = F^S \frac{2\rho_0}{\alpha_{hkl}\, q} \sin\left(\alpha_{hkl}\, q\, \frac{L}{2}\right)$$

This model have been applied to the analysis of several scattering patterns of the following systems: DLPE, DEPE, DOPE, DDAB lipids in water; GMO amphiphilic molecules with polaxamer P407 in water; $R_6^F\Sigma EO_2$ fluorinated surfactants in aqueous solutions and polimerized system formed in the CTAC with TEOS additives. The method presented in this dissertation provides a valuable tool which yields information on the micro- and meso-scopic structure of the cubic phases, on the phase coexistence, phase structural relationships and finally on the mechanisms of the phase transition kinetics.

Contents

1 Introduction

The small-angle x-ray and neutron scattering experiments are widely used to determine the symmetry and structure of self assembling systems. Still, in the case of the structures formed by a surfactant surface in binary (with water) and ternary (with oil and water) mixtures, it is often hard to exactly determine the topology of the phase formed in the system. The pioneering work in this field was done in 1968 by Vittorio Luzzati *et al* [1, 2, 3, 4]. They showed that the mesoscopic structure of surfactant aggregates could be more complex than spheres (micelles in microemulsion), cylinders (hexagonal phases) or planes (lamellar phases). In particular they observed a formation of periodic bicontinuous phases in amphiphilic systems (see chapter 1.2).

Scriven [5] was the first one to propose **triply periodic minimal surfaces** (TPMS) as a possible realization of the bicontinuous structures in these mixtures.

Since then the scattering techniques were often used to monitor the structural phase transitions, for example [6,10,7,8,9,10]. All these works indicate that the SAXS and SANS are powerful tools which in principle provide information on the symmetry and structure of the phases present in the system. Yet, the x-ray diffraction data are not always conclusive: due to the generally small number of reflections, an accurate reconstruction of an electronic map of the cubic cell is often impossible. **Even once the space group is rigorously established, there is still the question as to the identity of the minimal surface and thus the topology of the structure.** For example, the first report on the observation of a periodic surface in block copolymers was done in 1986 by Thomas *et al* [11]. They identified the surface dividing A monomer rich and B monomer rich domains as the Schwartz minimal surface D. It took nine years until Hajduk *et al* [12] in 1995 gave the correct identification of this structure as the G gyroid minimal surface. It proves, that even for structures of different space symmetry groups, exact determination of them may be very difficult.

Inspite of quite a long history of the studies of the triply periodic cubic phases in amphiphilic mixtures (see chapter 1.3) there is still an evident lack of simple models for the scattering amplitudes. This is probably due to the mathematical and geometrical complexity of the triply periodic surfaces (TPS). Yet as the cubic phases based on these surfaces are discovered in wider and wider span of systems and enter the realm of technology (see chapter 1.1) the theoretical analysis of these systems is more than needed.

In the introduction we will first introduce the concept of triply periodic surfaces (chapter 1.1) then the system of our interest is described (1.2) and finally a brief historical survey of the experimental scattering studies is presented (1.3).

1.1 Triply Periodic Surfaces

The periodic surface is the surface that moves onto itself under a unit translation in one, two or three coordinate directions similarly as in the periodic arrangement of atoms in regular crystals. The most interesting are triply periodic surfaces which are periodic in all three directions forming structures which have various crystallographic symmetries. In this work we will concentrate on smooth surfaces with cubic symmetry.

The paradigm structures for all periodic surfaces are minimal periodic surfaces. Such surfaces have zero mean curvature at every point of the surface as was shown by Meusnier [13] and Laplace in XVIII century. The simple patch of the minimal surface can be visualized in a simple experiment of Plateau (Belgian physicist XIX century): use a soap solution and dip a metal frame (not necessarily planar) in it. The film that forms on the frame will adopt the shape such as to minimize the surface free energy i.e. as to minimize the area of the surface (hence the name minimal surface).

The first periodic (in one direction only) minimal surface discovered in 1776 [14] was a helicoid: the surface swept out by the horizontal line rotating at the constant rate as it moves at a constant speed up a vertical axis. The next example (periodic in two directions) was discovered in 1830 by Herman Scherk. The first triply periodic minimal surface was discovered by Herman Schwarz in 1865. The revival of interest in periodic surfaces was due to the observation (Luzzati *et al* [1, 2, 3, 4]) that bilayers of lipids in water solutions form at suitable thermodynamic conditions triply periodic surfaces and the discovery of new triply periodic minimal surfaces by mathematician Schoen [15]. If we draw a surface through the middle of the triply periodic lipid bilayer it follows from the geometrical constraints that it must be a triply periodic minimal surface [16].

The self-assembled structures formed by lipids or surfactants in water solutions are used nowadays as templates for the three dimensional polimerization reaction leading to the mesoporous sieves [17], contact lenses [18] or bulk catalysts and this adds a technological dimension to the study of periodic surfaces. The formation of periodic surfaces in etioplast in plants and the usage of periodic surfaces for the crystallization of high molecular weight membrane proteins [19] shows that these surfaces are related to biological problems. After the discovery of various structures formed by carbon, i.e. wires, fullerens it has been also shown theoretically that the carbon atoms can be arranged to form triply periodic surfaces [20, 21]. In ionic crystals the points at which the electrostatic potential is constant, form the periodic surface; its symmetry can be determined by the symmetry adapted distribution of charges [22]. It is also shown that there is a very strong connection between chemical structures and periodic surfaces [23, 24].

1.1.1 Types of periodic surfaces

Triply periodic surfaces can be nodal ([25, 26, 27], [28]), equipotential surfaces ([29], [30]) and minimal surfaces. In this work we are interested only in minimal and nodal surfaces. They are briefly described below in terms of their geometrical properties and generating equations.

Surfaces are characterized locally by the mean H and Gaussian K curvature. K and H can be calculated according to $H = 1/2(1/R_1 + 1/R_2)$, $K = 1/(R_1 R_2)$, where R_1 and R_2 are principal radii of curvature (see Figure 1).

From the point of view of physics especially important are the ones of

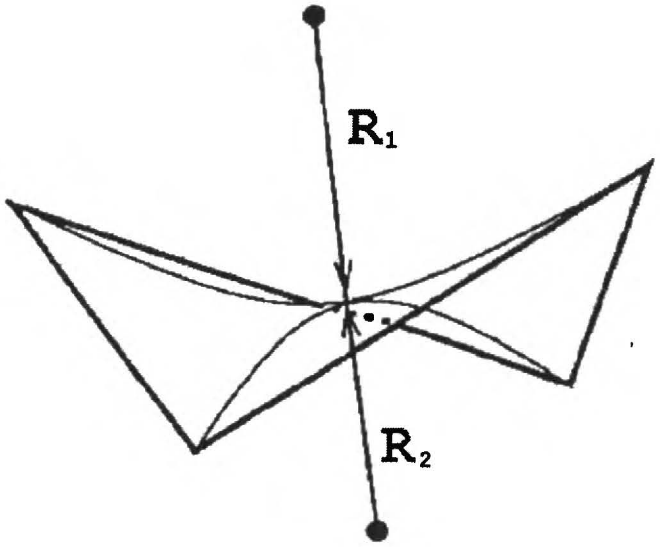

Figure 1: A piece of surface with non-positive Gaussian curvature. The two principal radii of curvature are shown. A minimal surface satisfies the condition $R_1 = -R_2$ at every point on the surface.

constant mean curvature since they are widespread in nature. A soap film spanned on a wire frame is a surface with zero mean curvature and a soap bubble is a surface of constant mean curvature. The curvature of the surface is related to thermodynamic quantities by the Poisson-Laplace equation $H = \Delta P/2\sigma$, where H is the mean curvature at the interface of two homogeneous media, ΔP is the pressure difference across the interface, and σ is the surface tension.

Every triply-periodic surface can be characterized by the genus, an integer number which describes the number of holes or handles in the surface. The

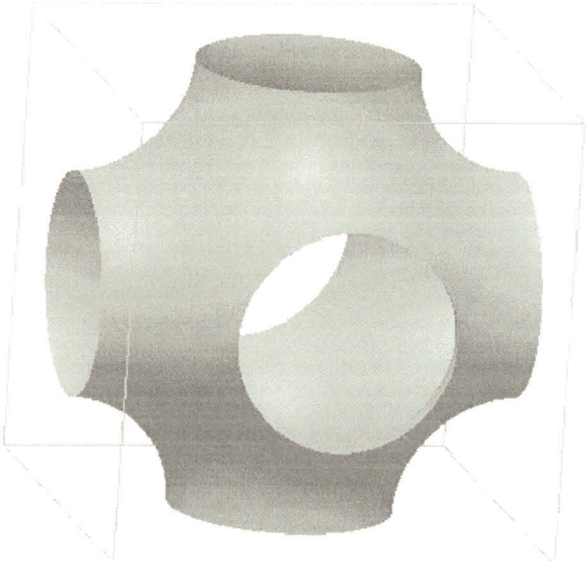

Figure 2: The unit cell of the P triply periodic minimal surface.

genus of a surface is related to its local properties by the Gauss-Bonnet theorem:

$$\int dSK = 2\pi\chi = 4\pi(1-g) \tag{1.1}$$

where K is the Gaussian curvature, χ the Euler-Poincaré characteristic, and g is the genus. It is possible that different surfaces have the same genus. The genera for the best known triply-periodic surfaces, reported for a translational unit cell are: 3 for Schwarz P, 5 for Schoen G, 9 for Schwarz D surface (2 for a smaller unit cell preserving the surface symmetry only). The cubic cells of these minimal surfaces are shown on Figures 2-4.

Periodic surfaces can also be characterized by a distribution of normal vectors. In the case of polimerized surfactant membranes such distribution

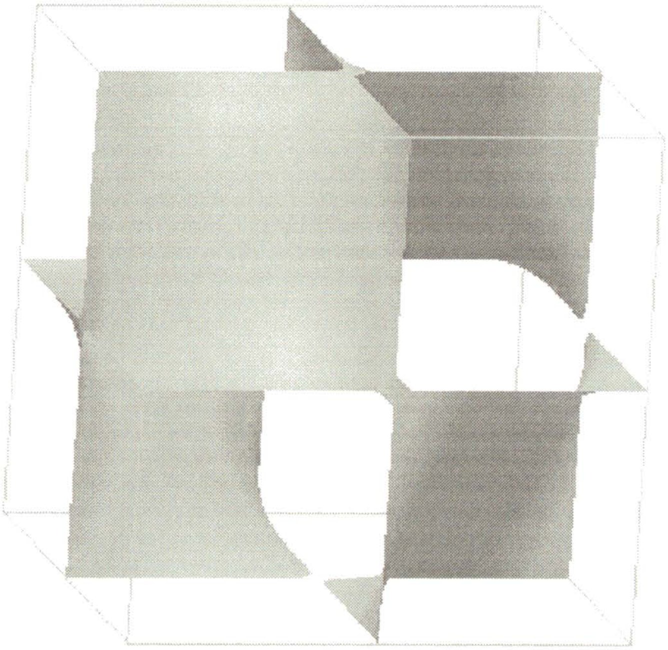

Figure 3: The unit cell of the D - double diamond TPMS.

is accessible experimentally via ^2H NMR technique ([31], [32]).

1.1.2 Minimal and constant mean curvature surfaces

Triply-periodic minimal surfaces (TPMS) are surfaces of constant mean curvature equal zero. The name "minimal" comes from the fact that the surface spanned on an sufficiently small frame has the lowest, "minimal" surface area if it is the surface of zero mean curvature. TPMS are infinite and are not bounded by a frame, but the mean curvature for these surfaces is zero at every point on the surface. That is why they are called "minimal". The condition of zero mean curvature implies that the Gaussian curvature is non-positive at every point. The points where the Gaussian curvature is zero are

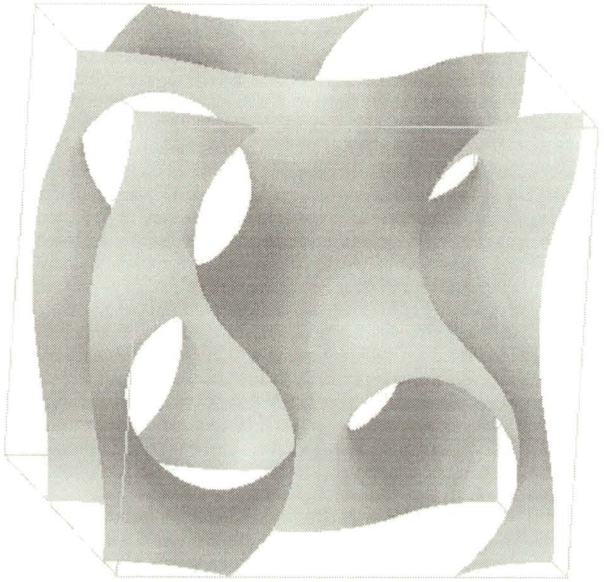

Figure 4: The unit cell of the G - gyroid TPMS.

called the flat points. These points are isolated.

Most of the TPMS divide the volume into two equal subvolumes (balanced surfaces - P,D,G are the most prominent examples). There are also TPMS which divide volume into unequal subvolumes (unbalanced surfaces - for example I-WP surface (Figure 5)).

TPMS are described locally by the Enneper-Weierstrass equations ([15], [33]):

$$
\begin{aligned}
x &= \tau Re \int_{\omega_0}^{\omega_1} d\omega e^{i\theta} R(\omega)(1-\omega^2) \\
y &= \tau Re \int_{\omega_0}^{\omega_1} d\omega e^{i\theta} R(\omega) i (1+\omega^2) \\
z &= \tau Re \int_{\omega_0}^{\omega_1} d\omega e^{i\theta} R(\omega) 2\omega
\end{aligned}
\tag{1.2}
$$

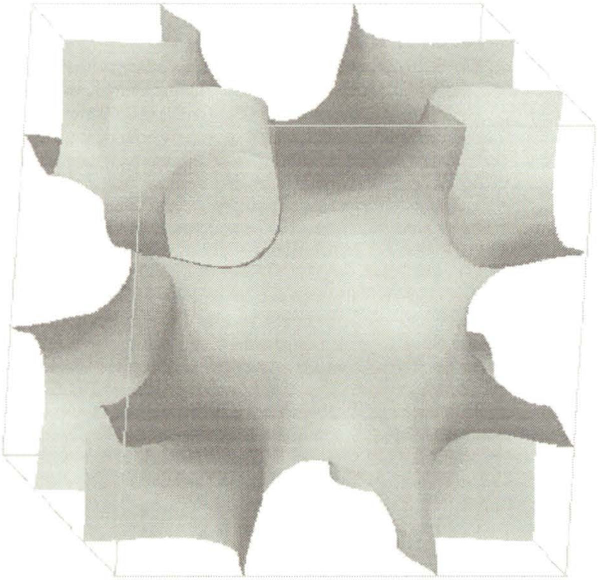

Figure 5: The unit cell of the I-WP TPS.

where *Re* denotes the real part of the complex integral and integration is carried on an arbitrary path from ω_0 to ω_1 in the complex plane. The Enneper-Weierstrass equations guarantee that the surface is minimal but not necessarily embedded i.e. free of self-intersections. $R(\omega)$ is called the Weierstrass function and is characteristic for a given minimal surface. The parameter τ sets the length scale. The angle θ is called the Bonnet angle. The transformation which results from the change of θ is called the Bonnet transformation. The surfaces related by Bonnet transformation are called associate. The Bonnet transformation is isometric and conformal, all the lengths and angles are preserved. The surface is only bent without stretching. The surfaces related by Bonnet angle equal to 90° are called adjoint or conjugate surfaces, since

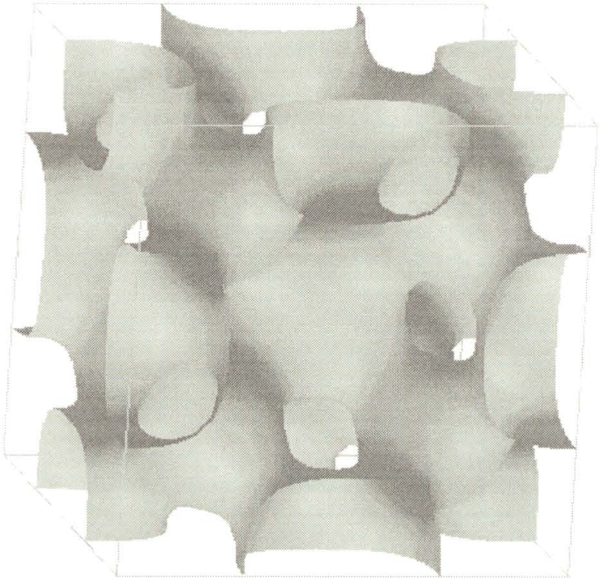

Figure 6: The unit cell of the F-RD TPS.

they are described by adjoined (conjugate) complex function. D, P, G are associate surfaces with the Weierstrass function $R(\omega) = (1 - 14\omega^4 + \omega^8)^{-1/2}$. The Bonnet angle is respectively $\theta = 0°, 90°, 38.015°$ [15]. Thus P and D are adjoint surfaces. The properties of the TPMS follow uniquely from the Weierstrass function $R(\omega)$ yet the $R(\omega)$ function is known only for few TPMS of simple topology.

Another method of obtaining the TPMS have been shown by Góźdź and Hołyst [34, 35]. The minimization of the Landau-Ginzburg potential in real space led to the discovery of many new TPS of the mean curvature close to zero.

TPMS belong to the broader class of periodic surfaces of non-zero con-

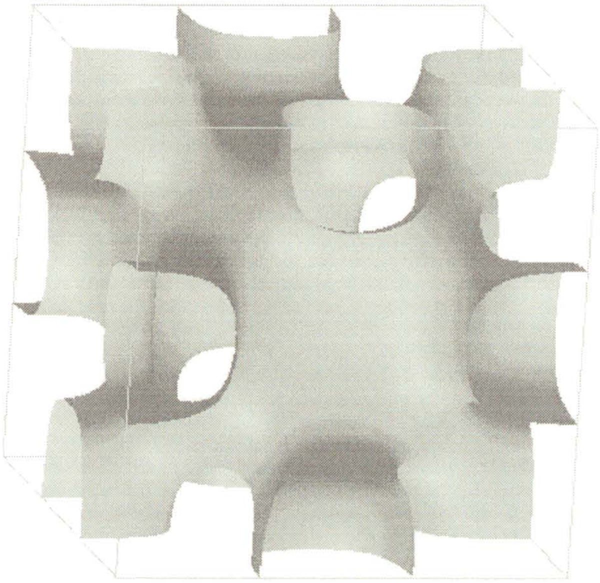

Figure 7: The unit cell of the C(P) TPS.

stant mean curvature (CMC). The existence of periodic CMC was proven in 1970 [36] for two doubly-periodic surfaces of hexagonal and square symmetry. First triply-periodic CMC surfaces were calculated numerically for P, D, I-WP, F-RD (Figure 6), C(P) (Figure 7), and S'-S" surfaces [37]. It is commonly assumed [38, 39] that the surfaces inclosing the lipid bilayers in cubic phases are a compromise between the CMC surfaces and so called parallel surfaces. This last class contains surfaces laying at a constant distance away from the minimal surface.

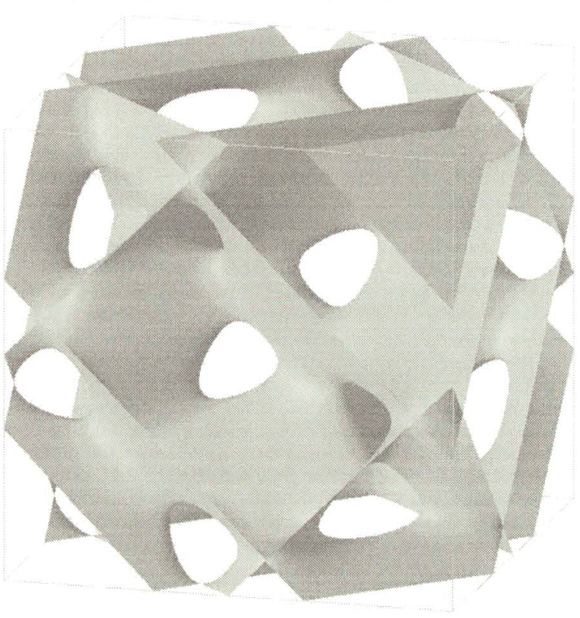

Figure 8: The unit cell of the C(D) TPS.

1.1.3 Nodal surfaces

The nodal surfaces are defined by $\Psi(\mathbf{r}) = 0$, for $\Psi(\mathbf{r})$ given by the following Fourier series ([25], [23])

$$\Psi(\mathbf{r}) = \sum_{\mathbf{k}} F(\mathbf{k}) \cos[2\pi \mathbf{k} \cdot \mathbf{r} - \alpha(\mathbf{k})] \tag{1.3}$$

where $\mathbf{k}$ describes the reciprocal lattice vectors for a given lattice, $\alpha(\mathbf{k})$ is a phase shift , and $F(\mathbf{k})$ is an amplitude associated with a given $\mathbf{k}$-vector.

Periodic surfaces can be approximated in terms of nodal surfaces. The quality of approximation depends on the number of terms in the Fourier series. The topology of a surface is in some simple cases already well reproduced by a series containing only the first terms in the expansion. Several such surfaces have been tabulated ([28] or [40]). For example the simplest approximations for P, D,and G surfaces based on Eq(1.3) are, respectively:

$$\cos(X) + \cos(Y) + \cos(Z) = 0 \tag{1.4}$$

$$\cos(X)\cos(Y)\cos(Z) + \sin(X)\sin(Y)\sin(Z) = 0 \tag{1.5}$$

$$\sin(X)\cos(Y) + \sin(Y)\cos(Z) + \cos(X)\sin(Z) = 0 \tag{1.6}$$

where $X = 2\pi x$, $Y = 2\pi y$, $Z = 2\pi z$. The nodal approximations for other four surfaces explored in this work are given in appendix 1.

Although the nodal surfaces are neither minimal nor constant mean curvature they can be used as an ansatz for such surfaces [41]. The huge advantage of the nodal surfaces is that they are described by simple mathematical equations. Equations generating the C(P), C(D) (Figure 8), F-RD and I-WP surfaces are given in Appendix 1.

1.2 Amphiphilic mixtures

The systems of our interest are the mixtures of water and surfactants - ***surface active agents.*** These are called binary mixtures. The models presented in this work apply also to ternary mixtures which consist of water, surfactant and additional hydrocarbons.

The mechanisms governing the self assembly of surfactant molecules and thus resulting in the fascinating wealth of phase behavior originate from two phenomena. One is the behavior of water itself the second being the complex construction of a surfactant molecule.

The unusual properties of water are well explained by the existence of the so called hydrogen bonds. The nature of a hydrogen bond is mainly electrostatic [42]. The bond is directional and forms along the covalent bond between the electro negative atom (the oxygen or nitrogen) and hydrogen. In a solid state the water molecules adopt a lattice where each oxygen is tetrahedrally coordinated to four other oxygens, with each hydrogen atom lying in the line joining two oxygen atoms forming linear sequence of a covalent and hydrogen bond ($O-H\cdots O$). Even though the structure of the liquid water is disordered the tendency to retain the ice-like tetrahedral network remains. When a molecule which cannot form the hydrogen bonds is inserted water molecules try to rearrange themselves around this foreign molecule in such a way as to preserve as many hydrogen bonds between water molecules as possible. If the nonpolar solute molecule is not too large, it is even possible for water molecules to pack around it without giving up any of their hydrogen bonds. Yet this reorientation is entropically very unfavourable because it imposes a new, more ordered structure on the surrounding water molecules. As a result the nonpolar hydrocarbon chains are very weakly solvable in water and hence their name - hydrophobic (*water hating*). On the other hand the polar compounds easily take part in creating the hydrogen bonds and water is a good solvant for them. That is why they are frequently referred to as hydrophilic (*water loving*) molecules.

The amphiphilic (*loving both*) molecule is composed of two covalently bound parts - a hydrophilic polar head and a hydrophobic hydrocarbon tail (see Figure 9). This complex construction of surfactant molecule induces a

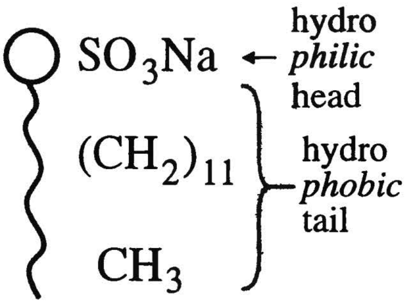

Figure 9: The amphiphilic molecule of a popular soap - sodium dodecyl sulfate (SDS).

rich phase behavior in mixtures with water. Namely the surfactant molecules will self arrange themselves into various structures preventing the contact between water and hydrocarbon chains. When also oil is added to the mixture, the amphiphilic molecules will create a surface boundary between water and oil rich regions. The simplest structure is a sack-like aggregate commonly called a micelle in which the polar heads cover the surface shielding hydrocarbon tails and molecules from contact with water. Another possibility is a surfactant bilayer. In this case the amphiphilic molecules form two palisades with the heads pointed outside towards water and the tails hidden behind them.

Depending on the thermodynamic and structural parameters of the system, such as temperature, composition, or length of an aliphatic chain in a surfactant molecule many different structures can be formed. The basic structures forming at low concentrations of surfactants are the spherical micelles, cylinders and plane surfaces. At higher concentrations these structures

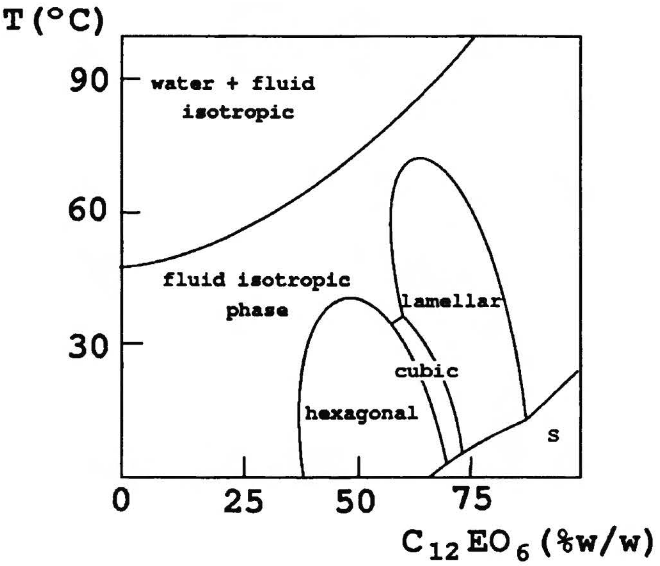

Figure 10: The phase diagram of a $C_{12}EO_6$/water mixture. Adopted from reference [45].

can order: micelles on the cubic lattice, cylinders on the 2D hexagonal lattice and plane membranes in lamellar phases. In a thin range of parameters the amphiphilic molecules arrange in the cubic liquid crystal phases.

The first phase diagram of a surfactant-water mixture was published by McBain in 1922 [43] (after [44]). Since then countless works on various surfactant and lipid systems were reported. A typical phase diagram of a binary mixture is shown on Figure 10. ($C_{12}EO_6$/water system [45]). Apart from the fluid isotropic phases the ordered ones appear. A lamellar phase exhibits a one dimensional order. It consists of plane sheets of water separated by surfactant bilayers (Figure 11a). At smaller surfactant concentrations a hexagonal phase is formed. It is made up of elongated cylinders with the

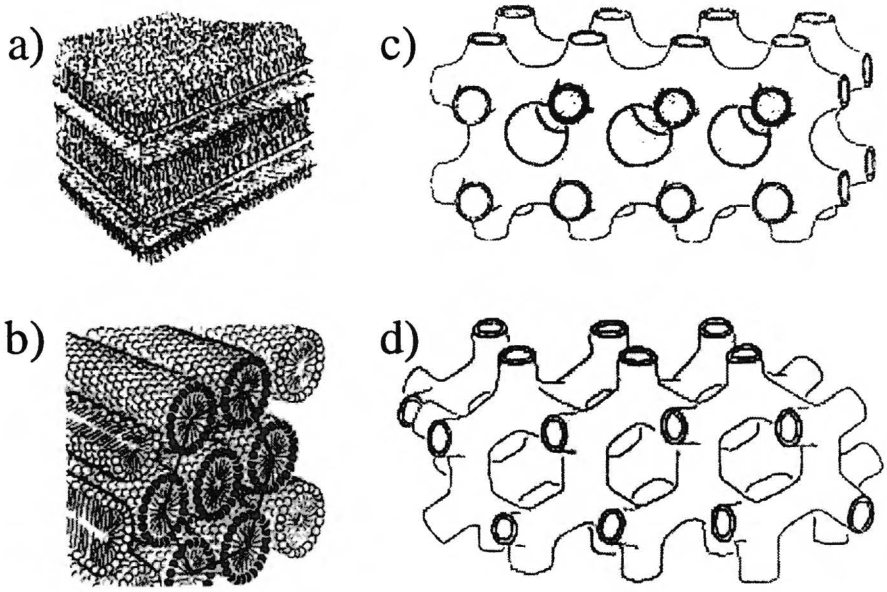

Figure 11: The lamellar (a), hexagonal (b) and cubic phases (P TPMS based (c) and D TPMS based (d)).

polar heads covering their surface. The cylinders are arranged in two dimensional hexagonal lattice (Figure 11b). It is quite common phenomenon that between the regions of hexagonal and lamellar phases a cubic phase domain is placed. The cubic bicontinuous phases (Figures 11c and d) consist of the surfactant bilayers which divide the volume into two mutually interwoven continuous but separate channels. Until now the existence of only three different continuous cubic phases have been confirmed. They are based on the P, D and G triply periodic surfaces. The nature and mechanisms of the phase transitions between the hexagonal and cubic and between the cubic and lamellar phases are still not well understood. Furthermore the world of triply periodic surfaces - potential templates for bicontinuous cubic phases in amphiphilic mixtures - is almost infinitely rich. These facts call for a detailed analysis of the structure of the cubic phases. Such analysis is needed also for determining the details of the cubic structures.

Another interesting subject is the cross sectional density distribution of a surfactant bilayer. There have been many extensive works conducted in this area. They deal with the hydrocarbon chain distribution within the layer (for example [46]) and the overall density distribution [47]. As was shown by Harper *et al* [39] the density profile of the bilayer can be determined also by an analysis of the x-ray spectra. A simple tool for such an analysis is presented in this work.

1.3 Scattering experiments on bicontinuous cubic phases

The first observation of a bicontinuous cubic phase in an amphiphilic mixture was reported by Luzzati and Spegt in 1967 [1]. The study concerned several water mixtures of various strontium soaps. Based on the x-ray diffraction data the structure of these phases have been assumed to compose of polar heads located on straight rods of finite length belonging to two interwoven infinite three dimensional networks. The hydrocarbon chains constituted a paraffin matrix in which the networks resided. The authors used this simple model of an $Ia\bar{3}d$ cubic phase to calculate the scattering intensities. This procedure led to a good qualitative agreement with the experimental pattern. In 1968 another works concerning this subject were published (for example

[2]). Again the rod model has been applied to fit the scattering spectra of $Ia\bar{3}d$ and $R\bar{3}m$ cubic phases.

In 1970 Scriven [5] pointed out that the energy minimization for the interface between components in amphiphilic mixtures may resemble one of the triply periodic surfaces. In 1980 Larsson [48] suggested that the x-ray diagrams of Lindblom [49] could be explained by a P TPS based phase. In 1983 Longley and McIntosh [50] explored a glycerol monooleate (GMO) water dispersion and basing on the x-ray data, suggested the D and G TPMS based phases.

The first calculation of the structure factors for a bicontinuous cubic phase based on a D - double diamond - TPS was conducted by Alan Mackay in 1985 [51]. Five years later Anderson *et al* [37] published an extensive work on triply periodic surfaces of prescribed mean curvature. One can find structure factors for the P, D and I-WP surfaces there. Since then, even though the atomic scattering curves had not been evaluated at that time, numerous works with a detailed analysis of the amphiphilic systems have been reported. The analysis of the scattering patterns was only qualitative and only the symmetry group was recognized. The analysis was based on the composition of the system and geometrical calculations leading to the surface areas per surfactant head. Good examples of such works are [52] (a study of a di-dodecyl alkyl-β-D-glucopyranosyl-*rac*-glycerol lipid water system), [53] (monoglyceride-Poloxamer 407-water system) or a technologically breaking through work on the polymerized mesoporous materials [54]. As it will be shown in the third chapter of this work (analysis of the x-ray patterns of the system presented in [53]) even a careful and detailed analysis conducted in this manner can lead to presumably wrong conclusions. The influence of the width of the layer decorating the base minimal surface on the scattering pattern is strong and thus the molecular factor should be included in studies concerning these systems.

An example of a comparison between theory and experiment involving the molecular factor (MF) associated with the width of the water or surfactant layer, is a very elegant work of M. Clerc and E. Dubois-Violette [55]. The authors presented an isotropic model of the MF and fitted the experimental data for several G - gyroid TPMS based systems. Although the fits were very promising, they were done only for the decorated G surface and its applicability for other structures has not been confirmed. Finally, only recently a beautiful work in this field has been done by P. E. Harper and S. M. Gruner [38, 39]. They have presented a detailed calculation of the scattering amplitudes for real lipid bilayers. From the data the authors have been able to reconstruct the bilayer's cross sectional density from the scattering intensities, assuming the reduction of the density for the terminal CH_3 methyl groups. Unfortunately their analysis is rather complex. Evaluation of the scattering amplitudes for a different system would include the whole procedure with Fourier transforms of the parallel surfaces. This is a mathematically and computationally demanding task and thus the method is not applicable as a common simple analysis tool for the x-ray data.

1.4 Summary of the scientific background and the aim of the work

As it has been shown in the introduction the binary and ternary mixtures of water and amphiphilic molecules have aroused a big theoretical and experimental interest over the last decades. The area becomes even more important as nano science enters the realm of technology.

In this work we will use the commonly accepted assumption that the cubic phases in amphiphilic mixtures are based on triply periodic surfaces. The science of these surfaces has been extensively reviewed in the first section of the introduction.

Looking at the theoretical works concerning the scattering patterns of these phases one sees a clear lack of simple models for the scattering amplitudes which would include the influence of the cross sectional density profile and fluctuations.

The purpose of this work is to fill this apparent gap in the theoretical studies and provide a simple tool for the theoretical analysis of the experimental data for the cubic periodic structures formed in the water mixtures of surfactants with hydrocarbons.

After the model will be derived (chapter 2) we will check its applicability by comparing the model intensities with experimental scattering patterns (chapter 3).

2 The model

The cubic phases made from the self assembled surfactant molecules with hydrocarbon chains in water solutions can be physically realized in two possible ways. One is a direct phase in which a water film is centered on the Triply Periodic Minimal Surface (in case of the C(P), C(D), F-RD and I-WP the TPMS is modeled here as a nodal surface[40]), while the two disjoint subspaces are filled with surfactant molecules (Figure 12b). The second possibility is an inverse phase where the TPMS is decorated by a surfactant bilayer and the two channels are filled with water (Figure 12c). In each case, knowing the microscopic details of the molecules present in the system, one can postulate the form of the cross sectional electron density profile $\rho(\xi)$ in the direction normal to the surface. A schematic drawing of these profiles for a normal and a direct phase is illustrated in Figure 12d and 12e. It is a good question whether a one dimensional density profile contains all of the information on the density distribution within a three dimensional cubic cell. It does when two assumptions are fulfilled. One is that the regions of a given species (surfactant heads, tails or water molecules) are contained within so called parallel surfaces (surfaces of a constant distance to the base minimal surface). Another possibility is that the bounding surfaces are the constant curvature ones. It is a subject of an ongoing dispute which of these two postulates is true. Still, as it was argued in [38] these two solutions are quite close to each other and assuming parallel surfaces should not introduce significant differences. The second assumption is that the one dimensional

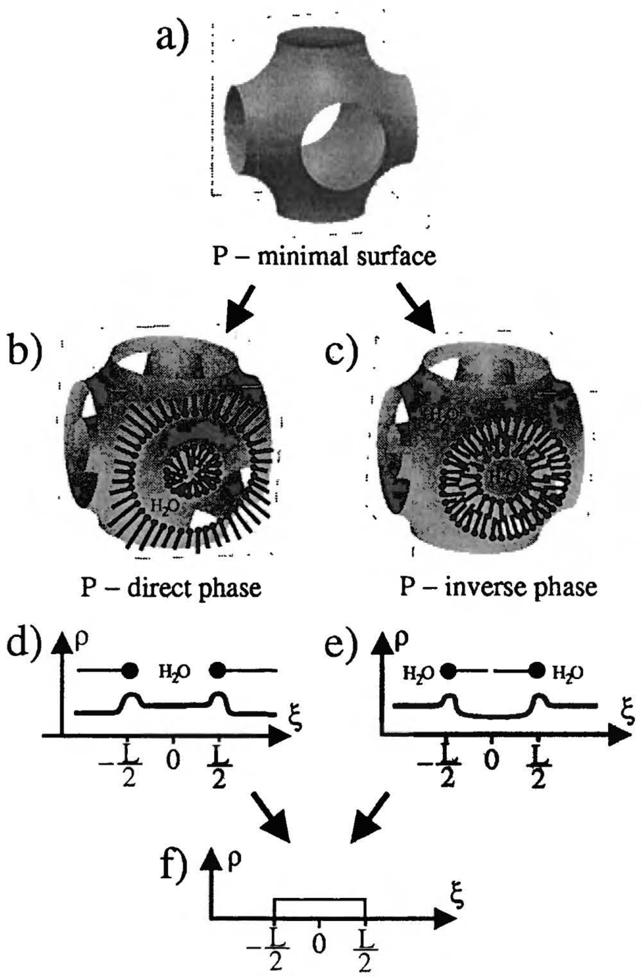

Figure 12: a) The zero width - mathematical surface in the unit cell of the P structure. The TPMS can be decorated by a water film b) - direct phase or by a lipid bilayer c) - inverse phase. These phases lead to different cross sectional density profiles d) and e) respectively. Still, in the first step approximation of the Small Angle X-Ray Scattering intensity these profiles can be modeled by f) a uniform density distribution. See text for explanation.

density profile does not change within the cubic cell. This is generally true due to the nature of the lipid or surfactant bilayers which are two dimensional fluids. Since the molecules can freely move along the membrane, any density fluctuations should be leveled on a very short time-scale. There still remains the dependence of the density profile on the local curvature which is not constant. Reference [39] contains a detailed study of this problem. Yet reconstructing the detailed density profiles requires an analysis that starts with fitting the spectra with amplitudes for a constant density distribution. Furthermore as it will be argued below and shown in our consecutive paper these matters will not affect the procedure leading to the determination of the most crucial parameters of a cubic phase. The last effect having an impact on the scattering amplitudes are the fluctuations of the membrane. They will be discussed in detail in chapter 2.3. For now it is enough to point out that characteristic relaxation times of both the molecular and collective fluctuations of the membrane are by many orders of magnitude shorter than typical exposition times in the scattering experiments. We will neglect all the correlations between fluctuations. It is thus enough to account for the fluctuations by introducing another parameter σ into the expression for the average density distribution. In general both the influence of the molecular and Debye-Waller term is dependant on the local curvature and orientation of the surface. Still as it will be shown in the following sections, inspite of the geometrical complexity of the TPMS based cubic phases, all of these effects factorize from the integral over the base surface and the scattering amplitude can be expressed as a product of a structure factor F^S, molecular factor F^M

and the Debye-Waller factor F^{DW}:

$$A(\mathrm{q}, \rho(\xi), \sigma) = F^S(\mathrm{q})\ F^M(\mathrm{q}, \rho(\xi))\ F^{DW}(\mathrm{q}, \sigma) \tag{2.1}$$

The main result of our work is summarized by the following formula:

$$A(\mathrm{q} \neq 0, \rho(\xi), \sigma) = F^S \left[2 \int_0^\infty d\xi \rho(\xi) \cos(q\ \alpha_{hkl}\ \xi)\right] \exp\left[-\frac{1}{2}(q\ \alpha_{hkl}\ \sigma)^2\right] \tag{2.2}$$

where ξ is the distance away from the base minimal surface, $\mathrm{q} = (2\pi/a)[h,k,l]$ is the scattering wave vector ($q = (2\pi/a)\sqrt{h^2+k^2+l^2}$), h, k, l are the Miller indices and σ is a standard deviation related to the fluctuations amplitude (see chapter 2.3). The normalized structure factors and the α parameters are explicitly given in tables 2-8 for the P, D, G, C(P), C(D), F-RD and I-WP TPMS based cubic phases. Thus *this formula allows an evaluation of the scattering amplitudes for any density profile* $\rho(\xi)$ *and fluctuations parameterized by the standard deviation* σ. The model scattering intensity for the powder samples is:

$$I(\mathrm{q}, \rho(\xi), \sigma) = \mathcal{M}_{hkl} |A(\mathrm{q}, \rho(\xi), \sigma)|^2 \tag{2.3}$$

where the multiplicity factor $\mathcal{M}_{hkl}$ is also included in the tables. *This method provides an easy to use tool which facilitates a very detailed determination of the actual cross sectional density profiles in the amphiphilic cubic systems.*

It is important to point out that expression (2.2) sets the normalization of the amplitudes in which the amplitude of the 000 reflection is equal to the total contrast electron density within the unit cell:

$$A(\mathrm{q} = 0) = \int_0^\infty d\xi\ \rho(\xi)\ [2s_0^\star a^2 + 4\pi\chi\ \xi^2] \tag{2.4}$$

where a is the cubic cell parameter, $s_0^\star = s_0/a^2$ is the dimensionless surface area of the base minimal surface per unit cell and is given by the structure factor for the 000 reflection ($s_0 = F_{000}^S$). The term in rectangular brackets gives the surface area of the parallel surfaces inclosing the subvolume of the layer decorating the base TPMS (see Eqn(2.8)). Both the surface areas of the base TPMS and their Euler characteristics χ per unit cell are summarized in Table 1 (chapter 2.1).

In many cases an even simpler analysis is needed. The cubic phases formed in self assembling systems have a growing potential for nanomaterial investigations and possible industrial applications. There, the key features of these phases like their type (direct-inverse) and the layer width L are of crucial importance. For example in catalytic applications the size of the pores have a dramatic influence on the efficiency and molecular selectiveness of the material. Since the main contrast is associated with the density difference between water and hydrocarbons, it is legitimate to assume a flat density profile for both cases (Figure 12f). In the scattering experiments only the intensity is measured, therefore the sign of the density difference can also be neglected and only the width L of the layer decorating the TPMS is important. Furthermore, as it will be shown in chapter 2.3, the fluctuations of the membranes have a minor influence on the relative intensity of the hkl peaks when compared with the influence of the layer width. Thus inserting a flat density profile $\rho(\xi)$ Eqn(2.11) and $\sigma = 0$ into Eqn(2.2) we obtain:

$$A(\mathrm{q} \neq 0, L) = F^S \frac{2\rho_0}{\alpha_{hkl}\, q} \sin\left(\alpha_{hkl}\, q\, \frac{L}{2}\right) \qquad (2.5)$$

where ρ_0 is the electron density within the layer and

$$A(\mathrm{q}=0,L) = \rho_0\, \phi(L^\star)\, a^3 \tag{2.6}$$

where ϕ is the volume fraction of the layer (see Eqn(2.7)). We will show in the third chapter that this simplified modeling leads to a good approximation for the intensity of the Bragg reflections and provides a very valuable insight into the details of the cubic phase structure.

Fitting of the model intensities given by substituting amplitude (2.5) into Eqn(2.3) to the experimental intensities provides the layer width L. In order to compute area per surfactant head for the direct and inverse structure of a given layer width L one can use the following formulas which relate the dimensionless layer width $L^\star = L/a$ with the volume fraction of the layer ϕ and the surface area of the interface between surfactant and water rich regions $s_{||}^\star = s_{||}/a^2$:

$$\phi = s_0^\star L^\star + \frac{\pi}{6}\chi L^{\star\,3} \tag{2.7}$$

$$s_{||}^\star = 2\, s_0^\star + \pi\chi L^{\star\,2} \tag{2.8}$$

In most cases comparison of the areas per surfactant head for the direct and inverse phase enables determination of which of the types has been formed. An example of such analysis is presented in the third chapter.

2.1 The Structure Factor

The structure factor (SF) arises from the base TPMS. It is given by:

$$F^S = \int_S d^2\mathbf{r}\exp\left[i\mathrm{q}\mathbf{r}\right] \tag{2.9}$$

where the integral is taken over the base minimal surface within the unit cell. In order to calculate the SF the surfaces have been triangulated. Then the integral over the surface has been substituted by a sum over the centers of the triangles:

$$F^S = \sum_{j=1}^{N} s_j \exp\left[i\mathbf{q}\mathbf{r}_j\right] \tag{2.10}$$

where s_j is the j-th triangle's surface area and $\mathbf{r}_j$ is the location of its center of mass. The structure factors for the 000 reflection give the surface area s_0 of the base TPMS. Thus the SFs have the dimension of surface area.

Table 1 summarizes the computed areas for the seven explored structures.

The list of all of the SFs for the strongest Bragg reflections are included in the Tables 2-8. As it was shown in [56] they are in a very good agreement both with the space symmetry group of the explored structures and with analytical evaluations for the P, D and G surfaces conducted by Mackay[51], Anderson [37] and Clerc and Dubois-Violette [55].

Values of the surface area of the base TPS for the C(P), C(D), F-RD and I-WP structures are slightly different then those given in literature. For example for the C(P) TPS we obtain a value of $s_0^\star = 3.7519$ while Anderson [37] provides $s_0^\star = 3.510$. Still our value is close to the one established by Schwartz [40] ($s_0^\star = 3.809$). These differences might be caused by the fact that Anderson has worked with minimal surfaces, while Schwartz (like in this work) has used its nodal approximation.

Major characteristics of the Triply Periodic Surfaces		
TPS	χ	$s_0^\star$
P	-4	2.3458
D	-2	1.9192
G	-8	3.0966
C(D)	-30*	4.4921
C(P)	-16	3.7519
F-RD	-40	4.8580
I-WP	-12	3.5543

Table 1: Data from numerical evaluations. χ is the Euler characteristic per unit cell and $s_0^\star = s_0/a^2$ is the dimensionless surface area of the TPS per unit cell with the cell parameter a.

* The value obtained by the the Euler relation for a triangulated surface. Please note that the best reconstruction of the volume fraction ϕ (Eqn(2.7)) and surface area of the parallel surfaces $s_{||}$ (Eqn(2.8)) is obtained for $\chi = -36$. It is the same value as reported by Landh [53].

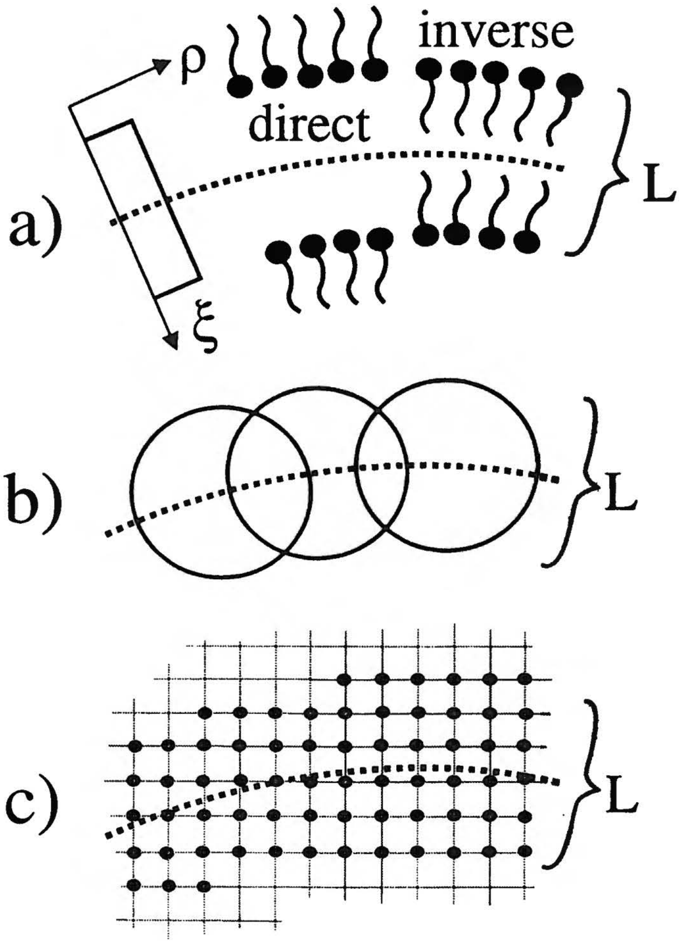

Figure 13: The visualization of the models used to evaluate the scattering intensities, a) shows schematically the base surface decorated either by water film (direct phase) or lipid bilayer (inverse phase) and the flat density profile, b) the isotropic model, c) the lattice model. See text for explanation.

2.2 The Molecular Factor

In order to evaluate the formula for a molecular factor (MF) we have first performed calculations for a flat cross sectional density profile (see Figure 12f):

$$\rho(\xi) = \rho_0 \Theta \left(\frac{L}{2} - |\xi| \right) \tag{2.11}$$

where ρ_0 is the density within the layer, Θ is the Heaviside step function ($\Theta(x) = 0$ for $x < 0$ and $\Theta(x) = 1$ for $x > 0$) , ξ is a coordinate along the direction normal to the base minimal surface - namely, it is the distance away from the minimal surface and finally, L is the width of the layer. Apart from the layer, the density is set to zero, thus the integral over the whole volume of the unit cell can be substituted by an integral over the subvolume inclosed between the parallel surfaces:

$$A(\mathbf{q}, L) = \int_V d^3\mathbf{r}\rho(\xi(\mathbf{r})) \exp[i\mathbf{q}\mathbf{r}] = \rho_0 \int_{V:|\xi(\mathbf{r})|<L/2} d^3\mathbf{r} \exp[i\mathbf{q}\mathbf{r}] \tag{2.12}$$

In order to perform this last integral numerically, the unit cell of each TPMS has been projected on a cubic grid $N \times N \times N$ of size $N = 96$ for the D surface, $N = 128$ for G and C(D) and $N = 192$ (P, C(P), I-WP and F-RD). For each point j on the grid, the smallest distance d_j to the surface has been calculated. Then the integral (2.12) has been evaluated as a sum over points laying in a distance d smaller then $L/2$ from the TPMS:

$$A(\mathbf{q}, L) = \frac{\rho_0 a^3}{N^3} \sum_{j:\, d_j<L/2} \exp\left[i\mathbf{q}\mathbf{r}_j\right] \tag{2.13}$$

A schematic visualization of this procedure is shown on Figure 13c. In order to check the accuracy of this method we have performed calculations for two

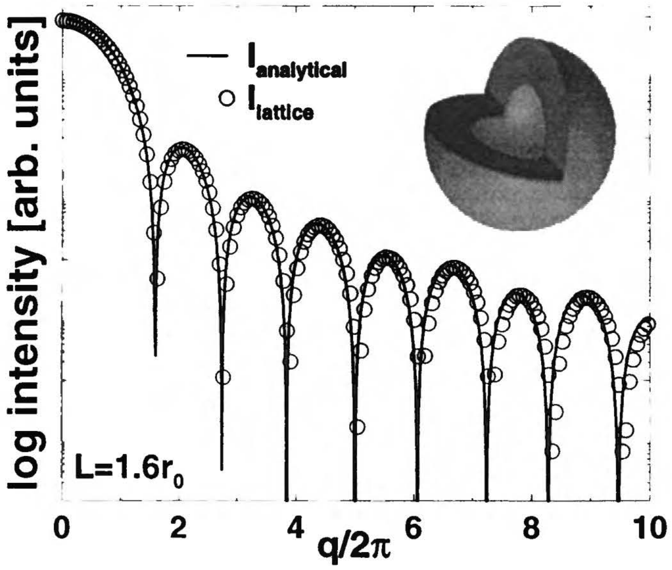

Figure 14: The scattering intensity as a function of the scattering vector length for a single layer of vesicles arranged on a 2D square lattice. The insert presents the vesicle.

analytically accessible structures - a vesicle and a rotational sinusoid. The results of this tests are presented in the following subsection.

2.2.1 A vesicle and a rotational sinusoid

Lets imagine a single layer of vesicles arranged on a 2D square lattice in the xy plane. It is important to remember here that it serves only as an abstract test structure for our model. Still this kind of thin layers of vesicles made from amphiphilic molecules have been obtained experimentally [57]. The vesicle is constructed by decorating a sphere of radius $r_0 = a/4$ by a layer of

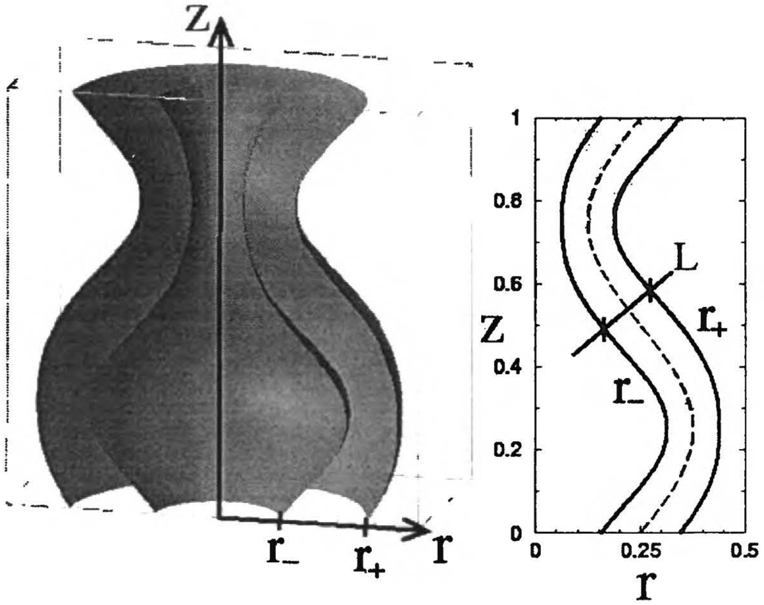

Figure 15: A cut through a unit cell of a rotational sinusoid. The structure is periodic in the z direction and is arranged on a 2D square lattice in the xy plane.

uniform density and width ranging from $L = 0$ to $L = a/2$. The analytical expression for the scattering amplitude reads:

$$A^{ves}(\mathrm{q}, L) = \frac{1}{L}\int_0^{2\pi} d\phi \int_0^{\pi} d\theta \sin\theta \int_{r_0-L/2}^{r_0+L/2} dr\, r^2 \exp\left[i2\pi l r \cos\theta\right] \qquad (2.14)$$

where for simplicity the lattice cell parameter has been set to unity ($a = 1$) and the scattering vector $\mathrm{q} = (2\pi/a)[h, k, l]$ is parallel to the z axis ($h = 0$ and $k = 0$). Figure 14 presents the scattering intensity as a function of the scattering wave vector. The lattice model reproduces the intensity evaluated analytically very well.

The sphere is a structure of positive Gaussian curvature (both principal radii of curvature have the same sign). The TPMS have negative Gaussian curvature meaning that at every point on the surface, the principal radii of curvature have opposite signs. Thus we have used another test structure that has both positive and negative Gaussian curvature regions. It is a rotational sinusoid (Figure 15). It's base surface is a cylinder of radius $a/4$ modulated by a sinus function. In the cylindrical coordinates the base surface is given by the following equation:

$$r = \frac{a}{4} + \frac{a}{8}\sin(2\pi z) \tag{2.15}$$

Again the base surface is decorated by a layer of uniform density and width $L \in (0, a/4)$. These kind of structures have been proposed for the intermediate stage in the kinetics of phase transitions between hexagonal and cubic structures (see for example [58]). The scattering amplitude:

$$A^{sin}(\mathrm{q}, L) = \frac{1}{L}\int_0^1 dz \int_0^{2\pi} d\phi \int_{r_-}^{r_+} dr\, r \exp\left[i\mathrm{qr}\right] \tag{2.16}$$

where $r_{\pm}$ are functions of z setting the boundaries of the layer in such a way that the layer width L is constant in the direction normal to the surface of the sinusoid. Figure 16 presents the comparison of the scattering intensity obtained analytically and numerically for the scattering vector $\mathrm{q} = q(2\pi/a)[1,1,1]$ and $L = a/4$. Again the lattice model reproduces it very well.

2.2.2 The isotropic fit

Our goal is to find a form of the expression for the scattering amplitude (Eqn(2.12)) that would factorize into a product of a structure factor and a

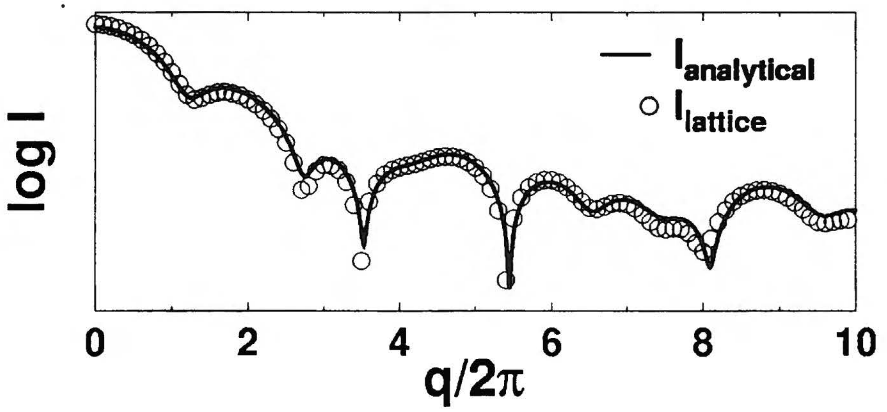

Figure 16: A comparison of the scattering intensity calculated analytically and numerically using the lattice model for a rotational sinusoid for the scattering vector equal to $\mathbf{q} = q(2\pi/a)[1,1,1]$.

molecular factor:

$$A(\mathbf{q}, L) = F^S(\mathbf{q})F^M(\mathbf{q}, L) \tag{2.17}$$

Dividing the left hand side of this equation (obtained numerically (Eqn(2.13)) by the appropriate structure factor we can extract an effective MF which was then fitted by a simple formula.

It appeared that the simple formula can be extracted from the model shown in (Fig. 13b). In its original form it was first proposed by M. Clerc and E. Dubois-Violette [55] and was successfully used to fit several scattering patterns of the simple gyroid, G, structure based phases. The idea is to decorate the TPMS with spheres of radius $L/2$ of a uniform density on the surface. This leads to an isotropic MF independent of the local curvature and orientation of the surface:

$$F^M_{iso} = \frac{2}{qa} \sin(qL/2) \tag{2.18}$$

This model reconstructs the Heaviside function form of the scattering density in the direction normal to the surface only for plane surfaces. In the case of the curved surfaces it is only an approximation which fails when the local radius of curvature is comparable with the layer width L.

We have found that for the uniform density distribution within the layer, the effective MFs of the explored TPMS based cubic phases can be very well approximated by a slightly corrected isotropic factor:

$$F^M(\mathrm{q}, L) = \frac{2\,\rho_0}{\alpha_{hkl}\, q} \sin\left(\alpha_{hkl}\, q \frac{L}{2}\right) \tag{2.19}$$

where the correction parameters α_{hkl} are characteristic for every Bragg reflection and are explicitly given for the most prominent reflections for the P, D, G, C(P), C(D), F-RD and I-WP structures in Tables 2-8. In this notation the MF has a dimension of electron charge per surface area. When multiplied by the SF of dimension of the area gives the final dimension of the scattering amplitude in arbitrary scale of electron charge. Please note here that it is exactly this form of the MF that has been inserted into the expression for the amplitude within the simplified model Eqn(2.5).

The details of fitting the isotropic MF to numerically obtained amplitudes are summarized in the following subsection.

2.2.3 Results for triply periodic surfaces

A typical powder diffraction pattern of a cubic phase in a binary or ternary mixture consists of few peaks. The number of the visible Bragg reflections rarely exceeds ten. To present the MF's for each structure we have chosen a certain number of the most pronounced reflections. To enter the list each peak had to be among the ten strongest ones for any layer volume fraction $\phi \in (0, \phi_{limit})$, where ϕ_{limit} was chosen to be equal to 0.8 for the P, D, G and I-WP structures, 0.65 for F-RD and C(D) and 0.5 for C(P). The layer's volume fraction ϕ is related to the layer width L by Eq(2.7).

In the case of the P, D and G structures the isotropic model works very well. The intensity dependence on the layer width L evaluated using this model is (except for a few peaks) the same as given by the numerical integral Eqn(2.13). However for the C(P), C(D), I-WP and F-RD surfaces, the numerical results differ significantly from the isotropic approximation and significant corrections (in terms of α_{hkl}) are needed in this case. A possible physical interpretation of the α_{hkl} parameters is the effective layer width seen in the cross section in the given hkl direction.

The Schoen P surface

The P surface has the $Im\overline{3}m$ symmetry group, its surface area per cubic cell is $s_0^\star = 2.3458$ and Euler characteristic $\chi = -4$. The P minimal surface is shown on Figure 2. Table 2 contains the structure factors for the minimal surface for the 20 most prominent Bragg reflections. Almost all of the examined reflections are very well described by the uncorrected isotropic model.

An example is shown in Figure 17. Even for large layer widths, the isotropic MF reproduces the numerically evaluated amplitude very accurately. Still two of the chosen peaks have to be slightly corrected. As an example we have plotted the amplitude of the 110 reflection as a function of the layer width L. In order to fit this dependence the isotropic MF required the alpha parameter $\alpha_{110} = 1.14$ (see Figure 18). The same figure contains the values of the 110 amplitude for three specific layer widths L computed by Harper [38]. As in the case of all the other eleven peaks presented there [38] the values are in excellent agreement with our computations.

Figure 19 shows how drastically the MF changes the relative intensities. One could imagine a binary water/surfactant system of a fixed volume composition 0.3/0.7. If the P phase have been formed, the direct phase would have the layer volume fraction $\phi \approx 0.3$ (upper diffraction pattern) while for the invert phase $\phi \approx 0.7$ (lower diffraction pattern). Thus comparing the numerical spectra with the experimental data one can unambiguously determine which structure has been formed. This result in turn can lead to the determination of many microscopic (such as the area per surfactant head) and macroscopic (such as the phase stability) characteristics of the system.

The Schwartz D - double diamond surface

The D surface (Figure 3) has the $Pn\bar{3}m$ symmetry. It is worth noting here that this is a unit cell for the surface only, while the symmetry of the two subspaces ($Fd\bar{3}m$) require an eighth times bigger unit cell (two times bigger linear size of the unit cell). Since we consider the scattering with the

The scattering data for the P based phases

hkl	$\mathcal{M}_{hkl}$	$F^{S\star}_{hkl}$	α_{hkl}	hkl	$\mathcal{M}_{hkl}$	$F^{S\star}_{hkl}$	α_{hkl}
0 0 0	1	2.3458		3 3 2	24	0.2795	1
1 1 0	12	-0.4496	1.14	4 2 2	24	0.2536	1
2 0 0	6	-0.5444	1	5 2 1	48	0.0861	1
2 1 1	24	0.4565	1.03	4 3 3	24	-0.2680	1
3 1 0	24	0.0985	1	5 3 0	24	-0.1693	1
2 2 2	8	-0.4056	1	5 3 2	48	-0.1356	1
3 2 1	48	-0.2177	1	6 1 1	24	0.1577	1
4 0 0	6	0.2454	1	5 4 1	48	0.1449	1
4 1 1	24	-0.2425	1	5 4 3	48	0.1795	1
3 3 0	12	0.2155	1	5 5 4	24	-0.2070	1
4 2 0	24	0.1580	1				

Table 2: The scattering data for the P structure. The first column contains the *hkl* indices, the second the appropriate multiplicity factors for a powder spectrum, the third the dimensionless structure factors $F^{S\star} = F^S/a^2$ for the zero-width base mathematical surface, the fourth the α_{hkl} correction parameters for the isotropic MF.

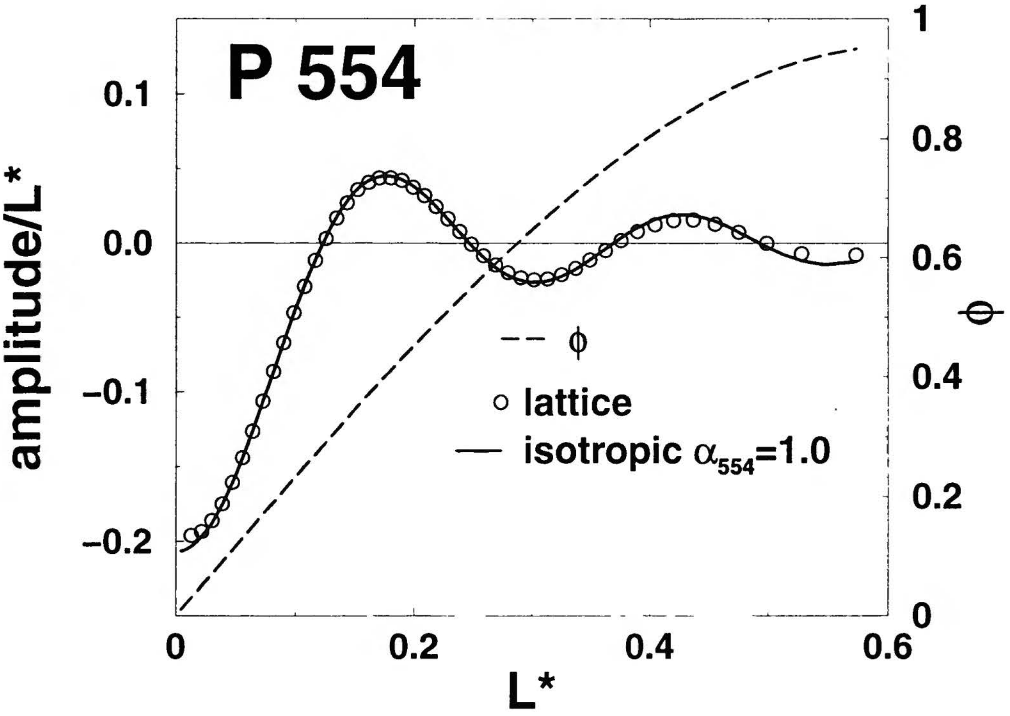

Figure 17: The P surface. The scattering amplitude of the 554 reflection plotted as a function of the dimensionless layer width $L^\star = L/a$, where a is the cubic cell parameter. The amplitude computed via the lattice (numerical) model is drawn with open circles and the amplitude given by the isotropic fit with $\alpha_{554} = 1.0$ with a solid line. The dashed line gives the layer volume fraction ϕ as a function of $L^\star$ (Eqn 3.12). The amplitude has been divided by $L^\star$ in order to compare it with the structure factor $(A(\mathrm{q}, L)/L^\star \to F^{S\star}$ when $L^\star \to 0)$.

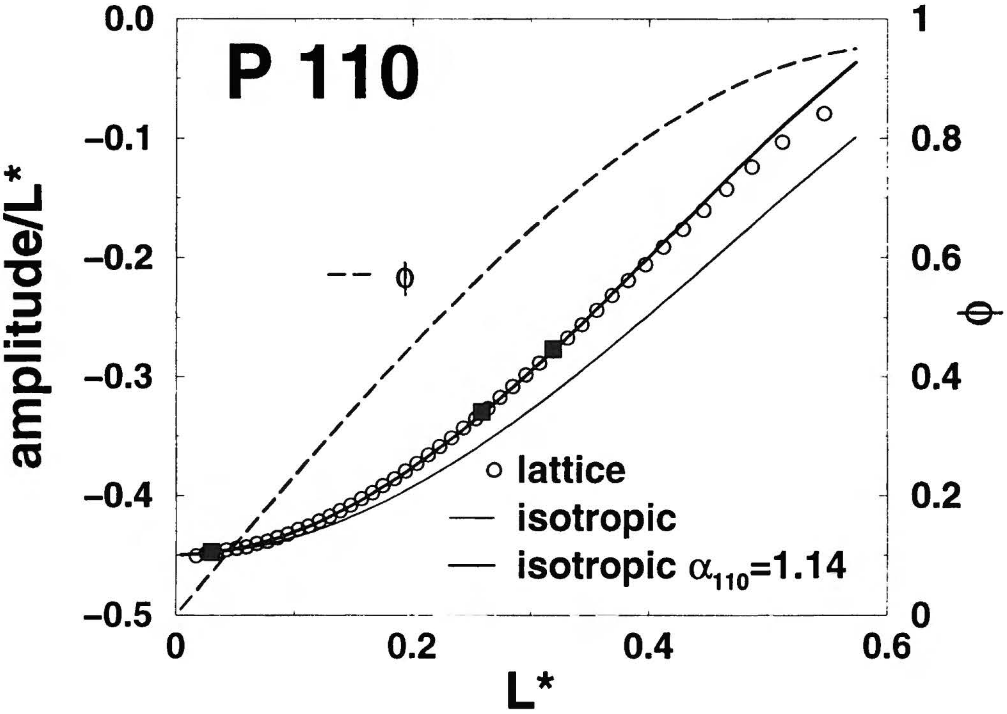

Figure 18: The P surface. The amplitude of the 110 reflection. The amplitude computed with the uncorrected isotropic MF is shown with the thin solid line while the corrected ($\alpha_{110} = 1.14$) fit is drawn with a thick solid line. The filled squares represent the amplitudes computed by Harper [38] for three volume fractions $\phi = 0.0766, 0.5791$ and 0.6998. As in the case of all the other 12 reflections presented in [38] the data is in very good agreement with the amplitudes computed via the lattice model (open circles). The layer volume fraction ϕ is given by the thick dashed line.

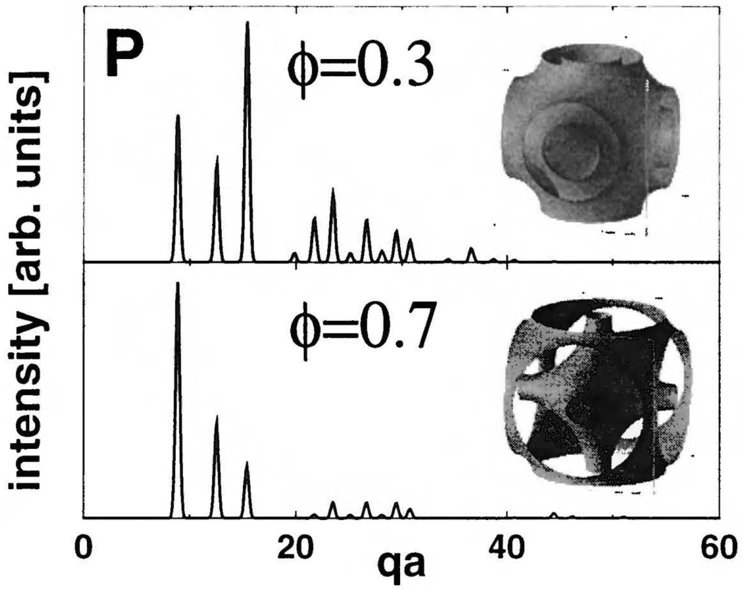

Figure 19: The scattering patterns for the P surface based cubic phases. The upper plot corresponds to the layer volume fraction $\phi = 0.3$ and the lower one to $\phi = 0.7$. The insets show the parallel surfaces within which the layer is confined.

surface contrast it is enough to take smaller unit cell, for which $s = 1.9192$, $\chi = -2$. Again as in the case of the P structure the effective MF's are very well described by the isotropic approximation. Only two reflections (110 and 200) display significant deviations from the isotropic model ($\alpha_{110} = 1.08$ and $\alpha_{200} = 1.09$). In case of all the other chosen reflections, within the numerical accuracy are equal to unity (see Table 3). Figure 20 shows the amplitude dependence on the layer width L for the 110 and 221 Bragg reflections.

The scattering data for the D based phases

hkl	$\mathcal{M}_{hkl}$	$F^{S\star}_{hkl}$	α_{hkl}		hkl	$\mathcal{M}_{hkl}$	$F^{S\star}_{hkl}$	α_{hkl}
0 0 0	1	1.9192			3 2 2	24	0.1862	1
1 1 0	12	0.4794	1.08		4 1 1	24	-0.1309	1
1 1 1	8	0.4851	1		3 3 1	24	0.1812	1
2 0 0	6	-0.2616	1.09		4 2 0	24	-0.1436	1
2 1 1	24	0.2120	1		4 2 1	48	-0.1084	1
2 2 0	12	0.2579	1		3 3 2	24	0.2094	1
2 2 1	24	0.2799	1		3 3 3	8	0.2203	1
3 1 0	24	-0.1885	1		4 3 2	48	0.1058	1
3 1 1	24	-0.0987	1		4 3 3	24	0.1600	1
2 2 2	8	0.2911	1		4 4 2	24	0.1481	1
3 2 1	48	0.0957	1		4 4 3	24	0.1722	1

Table 3: The scattering data for the D structure. The legend is the same as for Table 2.

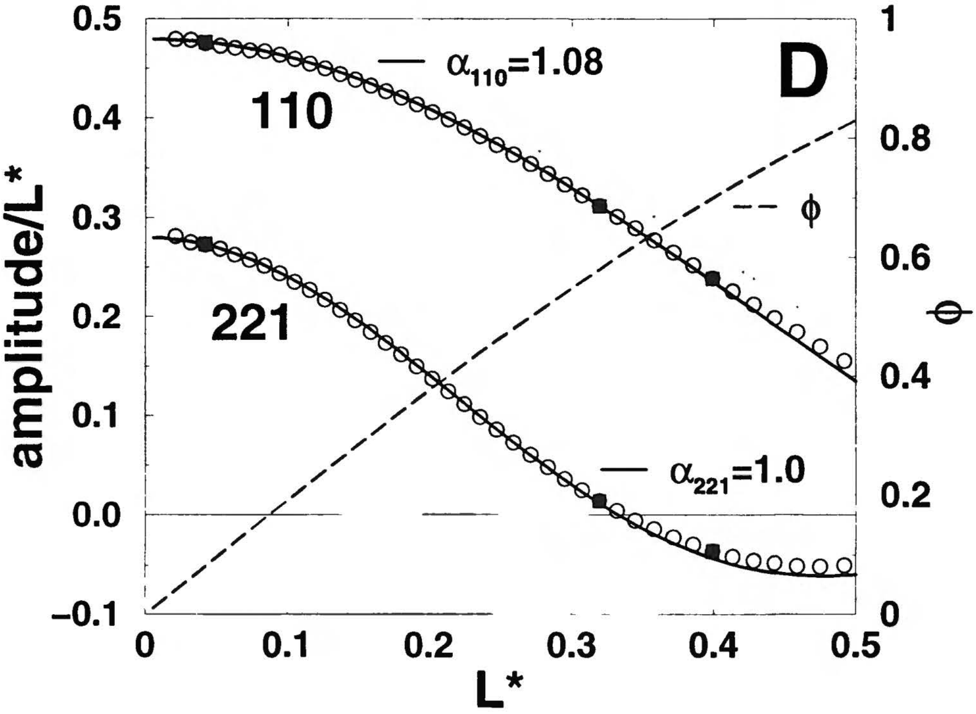

Figure 20: The D surface. The amplitudes of the 110 and 221 reflections. The lattice data is plotted with open circles. The filled squares present the amplitudes computed by Harper [38]. The amplitudes given by the isotropic model are drawn with solid lines. The thick lines correspond to the corrected MF ($\alpha_{110} = 1.08$ and $\alpha_{221} = 1.0$). In case of the 110 reflection also the uncorrected isotropic solution is shown (thin solid line). The layer volume fraction ϕ is given by thick dashed line.

The G - gyroid surface

The G surface (Figure 4) is of the $Ia\overline{3}d$ symmetry, $s = 3.0966$, $\chi = -8$. In the Table 4 we present the results of our fits. For most of the 21 Bragg reflections the isotropic model works excellently. Only four of the corrections parameters differed more then one percent from unity ($\alpha_{211} = 1.07$, $\alpha_{220} = 0.97$, $\alpha_{321} = 1.04$ and $\alpha_{400} = 1.04$). Figure 21 presents the numerical data together with the isotropic fits for the 211 and 611 reflections.

The C(D) - complementary to D surface

As in the case of the D structure for the surface contrast scattering computations it is enough to take one eight of the cubic cell. The surface space symmetry group is $Pn\overline{3}m$. For the smaller cubic cell (Figure 8) the normalized surface area $s = 4.4921$ and the Euler characteristic $\chi = -30$ ($\chi = -36$ should be used to reconstruct the volume fraction ϕ of the layer and the surface area $s_{||}$ of the parallel surfaces). Most of the 19 chosen reflections require corrections to the isotropic factor. Still the parameters α_{hkl} are sufficient to reconstruct the effective MF. The results for the C(D) structure are contained in Table 5. Figure 22 presents the results of fitting the isotropic form of the MF to the numerical data for the 111, 332 and 887 reflections.

The Neovius C(P) - complementary to P surface

The C(P) surface (Figure 7) is of the same symmetry as the P structure ($Im\overline{3}m$). In our calculations we have obtained the surface area per cubic cell $s = 3.734$. The C(P)'s Euler characteristic is $\chi = -16$.

The scattering data for the G based phases								
hkl	$\mathcal{M}_{hkl}$	$F^{S\star}_{hkl}$	α_{hkl}		*hkl*	$\mathcal{M}_{hkl}$	$F^{S\star}_{hkl}$	α_{hkl}
0 0 0	1	3.0966			5 4 1	48	-0.1652	1
2 1 1	24	0.6544	1.07		6 3 1	48	-0.1992	1
2 2 0	12	0.4306	0.97		4 4 4	8	0.4112	1
3 2 1	48	-0.0971	1.04		5 4 3	48	0.3012	1
4 0 0	6	-0.3375	1.04		6 4 0	24	-0.1722	1
4 2 0	24	-0.3309	1		7 5 2	48	-0.1915	1
3 3 2	24	0.4751	1		6 5 5	24	0.3112	1
4 2 2	24	0.2770	1		6 6 4	24	0.2403	1
4 3 1	48	0.1898	1		7 5 4	48	0.1700	1
6 1 1	24	-0.2287	1		7 7 6	24	0.2712	1
5 3 2	48	-0.1114	1		8 7 5	48	0.1715	1

Table 4: The scattering data for the G structure. The legend is the same as for Table 2.

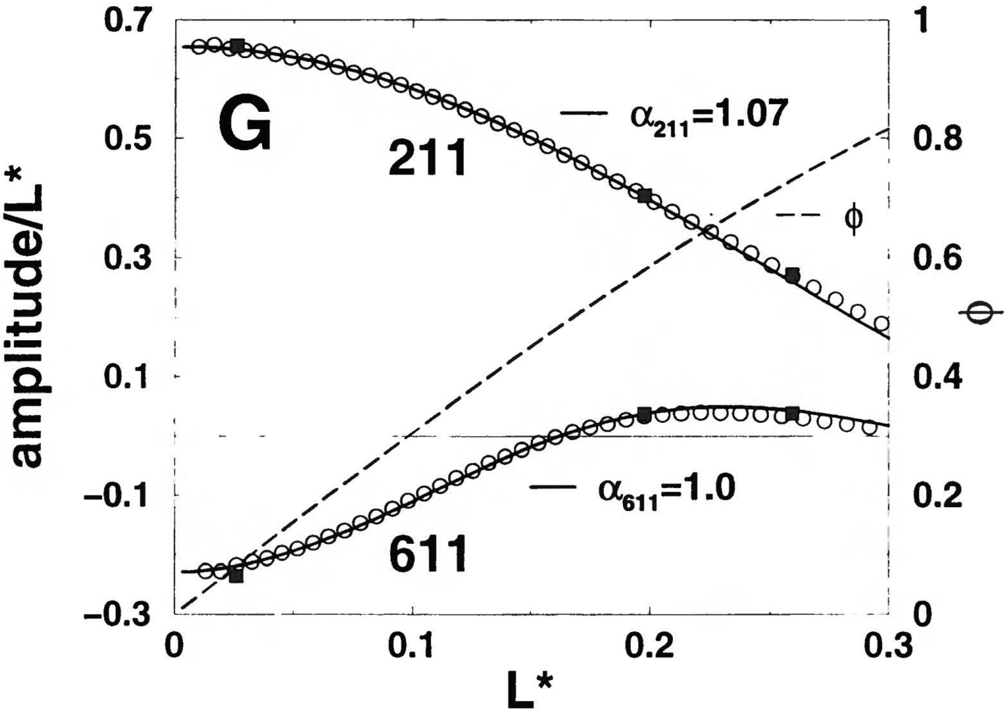

Figure 21: The G surface. A plot of the amplitudes of the 211 and 611 reflections. The legend is analogous to Figure 20.

The scattering data for the C(D) based phases								
hkl	$\mathcal{M}_{hkl}$	$F^{S\star}_{hkl}$	α_{hkl}		hkl	$\mathcal{M}_{hkl}$	$F^{S\star}_{hkl}$	α_{hkl}
0 0 0	1	4.4921			3 3 3	8	0.5463	1.05
1 1 0	12	0.2228	1.89		4 3 2	48	0.1846	0.97
1 1 1	8	-0.6489	1.7		5 2 2	24	-0.2825	1.15
2 0 0	6	-0.1303	0.84		4 4 1	24	-0.2547	1
2 1 1	24	-0.3337	1.13		4 3 3	24	0.2765	1
2 2 1	24	-0.5483	1.14		6 3 3	24	0.3577	1.04
3 2 1	48	-0.1474	0.92		5 4 4	24	-0.3589	1
4 0 0	6	0.2878	0.79		5 5 4	24	-0.3599	1
3 3 0	12	0.3785	1.09		6 6 6	8	0.6251	1
3 3 2	24	0.3726	1		8 8 7	24	-0.3430	1

Table 5: The scattering data for the C(D) structure. The legend is the same as for Table 2.

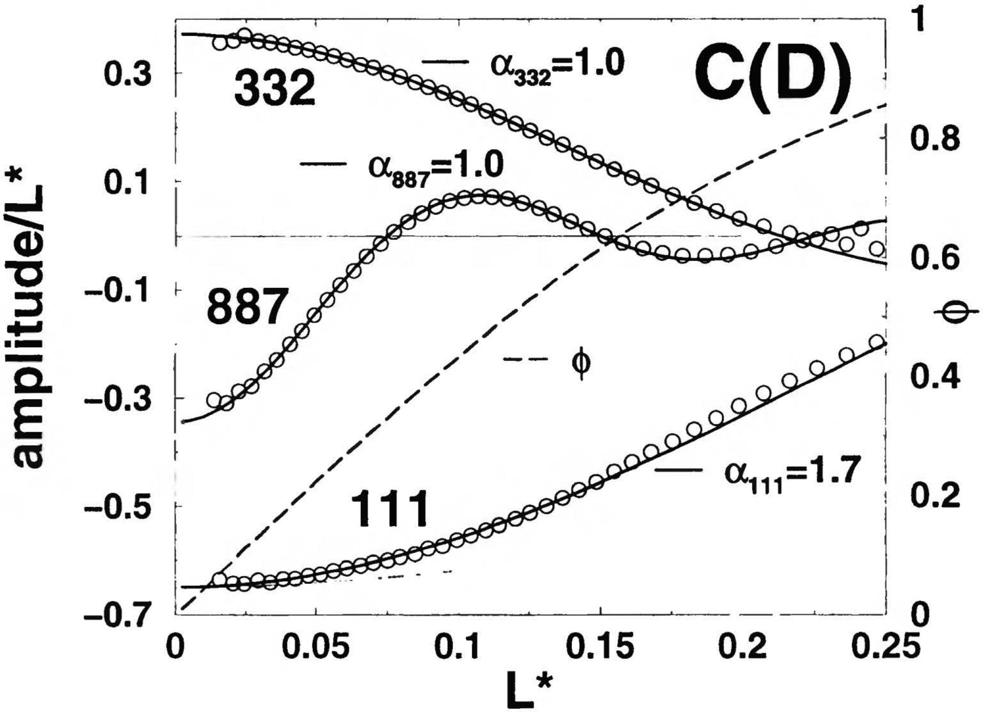

Figure 22: The C(D) surface. A plot of the amplitudes of the 111, 332 and 887 reflections.

Most of the C(P)'s 20 chosen peaks require corrections to the isotropic MF. The data for all of the peaks is included in Table 6.

The F-RD surface

The F-RD structure (Figure 6) of the $Fm\bar{3}m$ symmetry has the surface area $s = 4.887$ and $\chi = -40$. Most of the 20 chosen peaks require significant corrections to the isotropic model. The reconstructed MF's fit the lattice model data very well. The data is presented in Table 7.

The I-WP surface

The I-WP surface (Figure 5) has the $Im\bar{3}m$ symmetry. In our calculations we have obtained a value of $s = S/a^2 = 3.554$ for the surface area per side of the cubic cell. It's Euler characteristic is equal to $\chi = -12$. All of the 21 selected peaks have been successfully fitted with the modified isotropic MF. The data is presented in Table 8. Figure 23 presents the fits for the 200 ($\alpha_{200} = 1.23$) and 400 ($\alpha_{400} = 0.98$) reflections.

Comment to the results

The isotropic MF works very well for all three most commonly encountered structures P, D and G. Significant deviations from the isotropic model are seen when exploring the MF's of the more complex structures C(P), C(D), F-RD and I-WP. This is caused by the fact that the normal vector distribution of the simple surfaces, P,D,G is very similar to that of the sphere. Thus the real MF, which should in general be a function of the local curvature and orientation of the vectors normal to the base surfaces, when averaged

The scattering data for the C(P) based phases								
hkl	$\mathcal{M}_{hkl}$	$F^{S\star}_{hkl}$	α_{hkl}		*hkl*	$\mathcal{M}_{hkl}$	$F^{S\star}_{hkl}$	α_{hkl}
0 0 0	1	3.7519			5 2 1	48	-0.1448	1.0
1 1 0	12	-0.5076	1.5		6 0 0	6	0.4179	0.97
2 0 0	6	-0.3424	1.2		6 1 1	24	0.4737	0.97
3 1 0	24	0.5250	1.02		7 1 0	24	-0.4532	1.0
2 2 2	8	-0.6448	1.09		5 5 2	24	0.2769	1.05
3 2 1	48	0.1445	0.97		7 4 1	48	0.1796	1.0
4 0 0	6	-0.4870	1.13		8 3 1	48	-0.1889	1.0
4 1 1	24	-0.4699	1.04		9 1 0	24	0.3281	0.97
3 3 0	12	-0.4840	1.07		10 0 0	6	-0.6677	0.98
4 2 2	24	0.2527	0.97		13 1 0	24	-0.3705	1.0

Table 6: The scattering data for the C(P) structure. The legend is the same as for Table 2.

The scattering data for the **FR-D** based phases

hkl	$\mathcal{M}_{hkl}$	$F^{S\star}_{hkl}$	α_{hkl}	hkl	$\mathcal{M}_{hkl}$	$F^{S\star}_{hkl}$	α_{hkl}
0 0 0	1	4.8580		5 3 1	48	-0.1255	0.92
1 1 1	8	-0.4033	1.53	6 0 0	6	-0.3637	1.03
2 0 0	6	-0.8599	1.44	6 2 0	24	0.2526	1.0
2 2 0	12	-0.5387	1.08	6 2 2	24	-0.3813	1.0
3 1 1	24	0.3002	1.25	4 4 4	8	0.3859	1.0
3 3 1	24	0.2995	0.91	7 1 1	24	0.5348	1.0
4 2 0	24	0.5770	1.03	9 1 1	24	-0.3790	1.0
4 2 2	24	-0.1075	0.96	7 5 3	48	-0.2653	1.0
3 3 3	8	-0.8719	1.05	10 2 2	24	0.2699	1.0
5 1 1	24	-0.4983	1.06	12 2 0	24	-0.5034	0.99
4 4 0	12	-0.4920	1.13				

Table 7: The scattering data for the FR-D structure. The legend is the same as for Table 2.

The scattering data for the I-WP based phases

hkl	$\mathcal{M}_{hkl}$	$F^{S\star}_{hkl}$	α_{hkl}		hkl	$\mathcal{M}_{hkl}$	$F^{S\star}_{hkl}$	α_{hkl}
0 0 0	1	3.5543			4 4 0	12	0.2773	1.0
1 1 0	12	-0.2561	1.61		5 3 0	24	-0.3026	1.0
2 0 0	6	-0.5123	1.23		6 0 0	6	0.5253	1.04
2 1 1	24	-0.0986	0.74		4 4 2	24	-0.2423	0.97
2 2 0	12	-0.5006	1.0		5 3 2	48	0.2219	1.0
3 1 0	24	0.6608	1.05		6 1 1	24	0.2208	1.07
2 2 2	8	0.3980	1.16		6 2 2	24	-0.2594	0.96
3 2 1	48	-0.0919	1.03		7 2 1	48	0.1406	0.98
4 0 0	6	-0.3285	0.98		7 3 0	24	0.2657	1.0
4 2 0	24	0.2070	0.92		7 5 2	48	-0.2333	1.0
5 1 0	24	-0.3994	1.0		9 3 2	48	-0.2128	1.0

Table 8: The scattering data for the IW-P structure. The legend is the same as for Table 2.

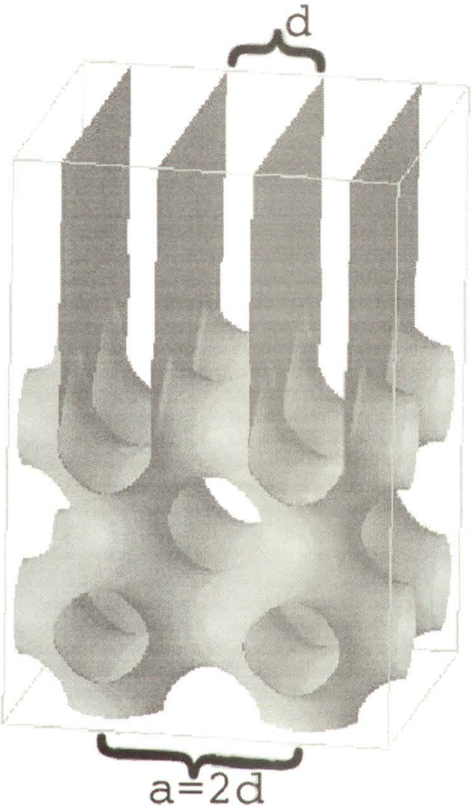

Figure 37: Schematic illustration of the lamellar to P TPMS based cubic phase transition and coexistence. The ratio between the cubic lattice constant a and the lamellar repeat distance d is indicated by the x-ray spectra [6].

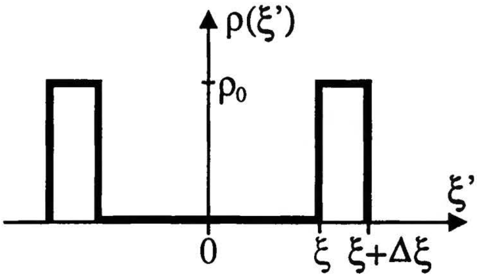

Figure 24: A model density profile for two thin layers of width $\Delta\xi$ laying in a constant distance ξ from the minimal surface. See text for explanation.

over the whole surface gives similar results as the isotropic model without corrections. This is not true in the case of more complex structures, where the parameter α_{hkl} has to be used for almost all of the Bragg reflections. Please note here that the biggest corrections apply always to the peaks of the smallest *hkl* indices.

2.2.4 The general form of the Molecular Factor

Having the MF for an uniform density within the layer one can compute the MF for a more complicated density profile. Lets imagine a structure composed of two thin layers of uniform density of scatterers ρ_0 of width $\Delta\xi$ laying in a constant distance ξ from the minimal surface (see Figure 24). The cross sectional density distribution $\rho(\xi')$ of this structure can be written as a combination of two Heaviside functions:

$$\rho(\xi') = \rho_0 \left[\theta(\xi + \Delta\xi - |\xi'|) - \theta(\xi - |\xi'|)\right] \tag{2.20}$$

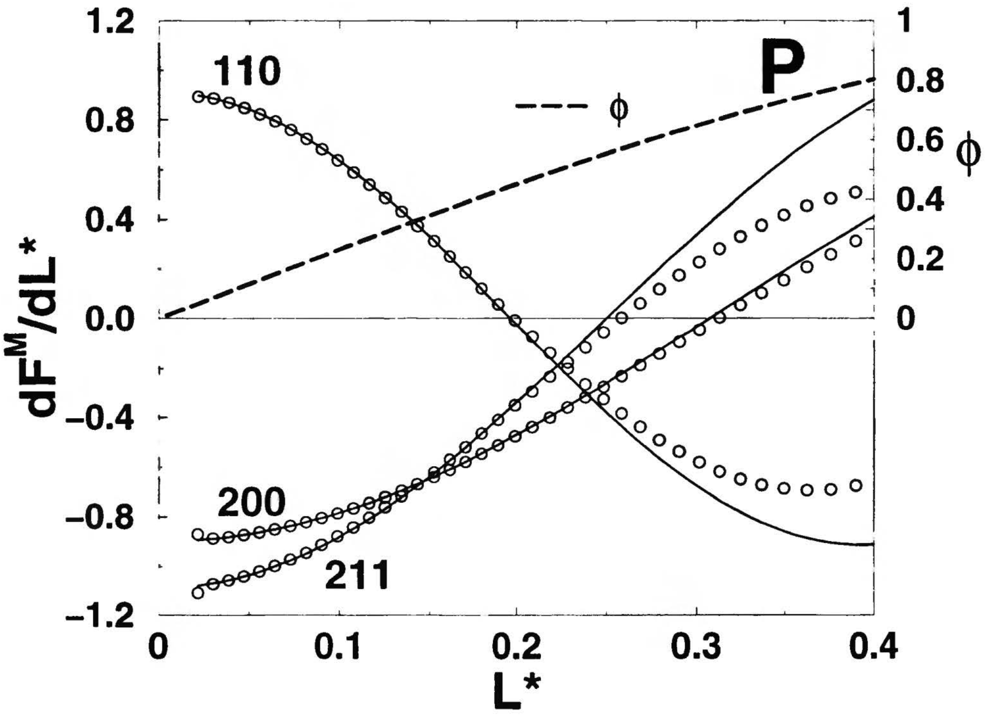

Figure 25: The numerically evaluated amplitudes for scattering on zero width parallel surfaces laying in distance $L/2$ away from the minimal surface are plotted with open circles. The solid lines are given by the relation Eqn(2.22) for $\rho(\xi) = 1$ with the same α parameters as the ones fitted through the integral relation Eqn(2.19).

Now using Eqn(2.5) with $\xi = L/2$ we can write the expression for the amplitude:

$$\Delta A(\mathrm{q}, \xi) = F^S \frac{2\,\rho_0}{\alpha_{hkl}\,q} \left[\sin\left(\alpha_{hkl}\,q\,(\xi + \Delta\xi)\right) - \sin\left(\alpha_{hkl}\,q\,\xi\right)\right] \tag{2.21}$$

And for $\Delta\xi \rightarrow 0$:

$$dA(\mathrm{q}, \xi) = F^S \frac{dF^M}{d\xi} d\xi = F^S\, 2\,\rho_0 \cos(\alpha_{hkl}\,q\,\xi)\, d\xi \tag{2.22}$$

This last expression when integrated with a Kronecker delta distribution centered at distance ξ from the minimal surface can be compared with numerical evaluations of the scattering amplitudes for zero width parallel surfaces. This has been done by triangulating the parallel surfaces and evaluating expression similar to the one for the SF (Eqn(2.10)). This provides an alternative way of establishing the α parameters. In the case of all of the seven explored structures the this test provided excellent agreement of the α correction parameters. However, as can be seen on Figure 25, the fits have a smaller range of applicability. The fits for the integral relation Eqn(2.19) works very well for the volume fractions up to $\phi \approx 0.8$ in case of the P,D,G structures and up to $\phi \approx 0.7$ in case of the others. The differential relation is fitted well in the range of $\phi \in (0, 0.6)$.

Having the expression Eqn(2.22) for the scattering amplitudes on parallel surfaces we can reconstruct the scattering amplitude for any cross sectional density distribution $\rho(\xi)$ of the layer decorating the base minimal surface:

$$A(\mathrm{q}, \rho(\xi)) = F^S\, 2 \int_0^\infty dl\; \rho(\xi)\; \cos(\alpha_{hkl}\,q\,\xi) \tag{2.23}$$

2.3 Debye-Waller factor

The last effect that have to be accounted for are the fluctuations of the membrane. We will assume only fluctuations in the direction normal to the surface of the layer and no correlations between the fluctuation amplitudes. First kind of the fluctuations are those of a single molecule. Due to the amphiphilic forces that are responsible for separation of water and hydrocarbon rich regions, the amplitude of the fluctuations of a single molecule is much smaller than the amplitude of the collective movements of the bilayer. We will parameterize both amplitudes by standard deviations σ_{single} and $\sigma_{collective}$. Since the total amplitude is

$$\sigma = \sqrt{\sigma^2_{single} + \sigma^2_{collective}} \tag{2.24}$$

in the first approximation we can neglect the fluctuations of a single molecule.

To evaluate the impact of the fluctuations we have assumed that they cause a broadening of the density profile described by a convolution of the original density profile $\rho(\xi)$ with a Gaussian distribution function with a standard deviation σ:

$$\rho_f(\xi, \sigma) = \frac{1}{\sigma\sqrt{2\pi}} \int_{-\infty}^{\infty} d\xi' \, \rho(\xi') \exp\left[\frac{-(\xi - \xi')^2}{2\sigma^2}\right] \tag{2.25}$$

An example of such a broadening is presented in Figure 26. Since we already have a formula for the scattering on any density profile (Eqn(2.23)) we can insert this broadened density distribution $\rho_f(\xi, \sigma)$ into Eqn(2.23) and obtain:

$$\mathcal{A}(\mathrm{q}, \rho(\xi), \sigma) = F^S \frac{2}{\sigma\sqrt{2\pi}} \int_0^{\infty} d\xi \int_{-\infty}^{\infty} d\xi' \, \rho(\xi') \exp\left[\frac{-(\xi - \xi')^2}{2\sigma^2}\right] \cos(\alpha_{hkl} \, q \, \xi) \tag{2.26}$$

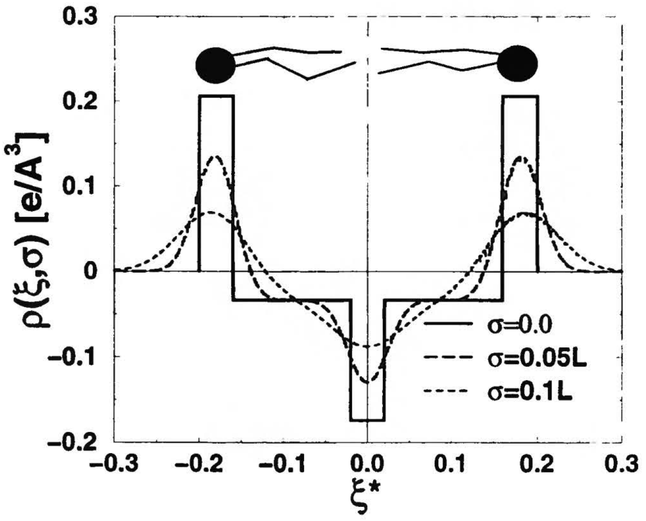

Figure 26: The cross sectional density profile used in the computations of P. E. Harper and S. M. Gruner [38] for a phospholipid molecule is shown with a solid line. The density distribution for fluctuations with amplitude parameterized by standard deviation $\sigma = 0.05L$ is shown with a dashed line, and $\sigma = 0.1L$ with a dotted line.

and after some analytical transformations (see Appendix 2) it can be expressed as

$$A(\mathrm{q}, \rho(\xi), \sigma) = F^S \left[2 \int_0^\infty d\xi \; \rho(\xi) \; \cos(q \; \alpha_{hkl} \; \xi)\right] \exp\left[-\frac{1}{2}(q \; \alpha_{hkl} \; \sigma)^2\right] \tag{2.27}$$

We find that the influence of the fluctuations is independent of the original density profile $\rho(\xi)$. The Debye-Waller term is expressed in a very simple form:

$$F^{DW}(\mathrm{q}, \sigma) = \exp\left[-\frac{1}{2}(q \; \alpha_{hkl} \; \sigma)^2\right] \tag{2.28}$$

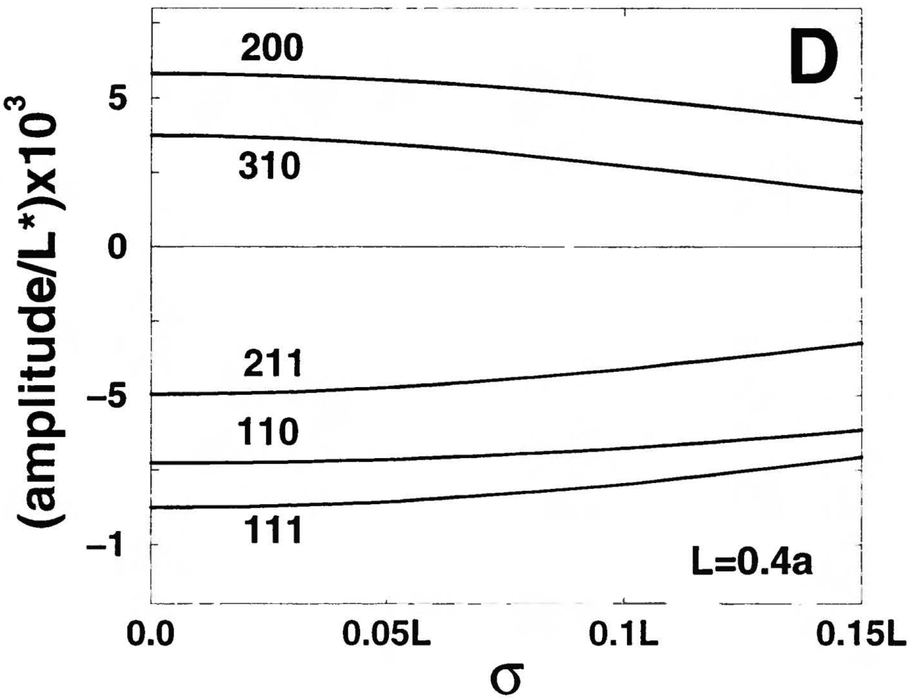

Figure 27: The impact of the fluctuations on the scattering amplitudes of the D TPMS based phase with a cross sectional density profile shown on Figure 26.

Thus equation (2.27) is the final expression for the scattering amplitudes and it is exactly this formula which was presented as the general model (Eqn(2.2)).

In order to inspect the influence of the Debye-Waller term we have performed calculations for a detailed cross sectional density profile presented in the work of P.E. Harper *et al* [38]. The authors used the Fourier transform of the volume enclosed between parallel surfaces (to the base minimal surface) to compute the scattering amplitudes for a bilayer made of typical phospholipid molecules. The width of the head group layer was set to 2/10 of the monolayer width ($L/2$). The hydrocarbon tail length was 7/10 of $L/2$ and finally the terminal methyl groups were said to occupy a layer of width equal to 1/10 of $L/2$. The electron densities were $0.54e/\mathrm{\AA}^3$, $0.3e/\mathrm{\AA}^3$ and $0.16e/\mathrm{\AA}^3$ respectively. After subtracting the electron density of water ($0.33e/\mathrm{\AA}^3$) the relative densities were 21/-3/-17 for head/tail/methyl groups (see Figure 26). Figure 27 shows the influence of the fluctuations on the scattering amplitudes for a D TPMS based cubic phase. It is in agreement with our previous work [56] that the decrease of the intensity of the Bragg reflections associated with the fluctuations is small. Even for large fluctuations amplitude $\sigma = 0.1L$ (see Figure 26) the decrease of the intensity is of the order of 10-20%. At the same time the dependence on the layer width is much stronger. For example the intensity ratio of the 211 peak to the 110 peak of the P TPMS based phase is $I_{211}/I_{110} = 1.6$ for the volume fraction $\phi = 0.3$ and $I_{211}/I_{110} = 0.2$ for $\phi = 0.7$ (see Figure 19).

3 Analysis of the experimental scattering spectra

In the preceding chapter we have presented the data for the scattering intensities of the strongest reflections for seven (P, D, G, I-WP, C(P), C(D) and F-RD) Triply Periodic Minimal Surface (TPMS) based cubic phases. In this chapter we want to show applications of the theoretical model for the scattering intensities to the analysis of the experimental spectra.

We have applied our method to several systems out of which nine are presented in this work. We have classified the systems into five groups. The first one includes the DLPE, DEPE and DOPE lipid aqueous dispersions. These lipid molecules are a part of a large class of lipids containing the -phosphatocholine part. They are commonly used to explore the phase diagrams of amphiphilic mixtures. Another example of a very popular amphiphilic molecule is the monoglyceride (GMO). We present a study of two systems with GMO. The third compound that has attracted a lot of experimental attention is the DDAB lipid (analysis of one such system is presented here). We decided to include also a fit for the scattering pattern of a polimerized structure formed in CTAS with TEOS additives. This study is motivated by a growing scientific and technological interest in microporous and mesoporous materials formed on surfactant templates by the polimerization of silicates (like TEOS). Finally we study a scattering pattern for a cubic phase of the $R_6^F\Sigma EO_2$ fluorinated surfactant in water.

As it will be discussed in detail in section 3.2, the analysis yielded interesting insight into the explored structures. In two cases we have discovered the phase coexistence between cubic-lamellar and cubic-hexagonal phases and established the epitaxial relations between them. The method has also been applied to a system of a known phase coexistence of a P and D structures observed in a fast cooling (0.5 degree per minute) temperature scan experiment. In this example we extract from the full x-ray spectrum the part of it which corresponds to the third unknown phase (probably metastable) forming during the phase transition. In principle such analysis shed light on the kinetics of phase transitions between ordered phases.

Fitting the scattering pattern provides not only the TPMS on which the cubic phase is based but also its macro- and mesoscale characteristics such as: layer width (decorating TPMS), volume fractions of the coexisting phases, area per head of a surfactant molecule, and composition of the cubic phases in the presence of the excess water in the system. Scattering patterns give also, in many cases, a clear distinction between a direct or an inverse structure. This in turn, together with the layer width L can be used to study the elasticity constants of a surfactant layer, preferred curvatures and conformations of the hydrocarbon chains inside the layers.

Section 3.1 contains a step by step description of the method. The results of its application are inclosed in section 3.2.

3.1 The method

In this section we want to present a detailed step by step approach towards analysis of the experimental scattering spectrum. In order to compare measured intensities with the modeled ones, we have to take into account the corrections due to the experimental setup. The first one is the Lorentz-polarization (LP) factor. It's form depends on the type of detector used to measure the scattering intensities. For a powder sample and a one dimensional detector, the LP reads [59]:

$$LP^{1D}(\theta_{hkl}) = \frac{1}{2}\left(\frac{1+\cos^2 2\theta_{hkl}}{\sin 2\theta_{hkl}}\right), \tag{3.1}$$

were θ_{hkl} is the scattering angle, related to the scattering vector $\mathbf{q} = (2\pi/a)[h, k, l]$ by the formula:

$$\sin\theta_{hkl} = \frac{\lambda q}{4\pi}. \tag{3.2}$$

Here λ is the wavelength of the radiation and a is the lattice parameter of the unit cell (linear size). For a two dimensional detector the LP has a slightly different form:

$$LP^{2D}(\theta_{hkl}) = \frac{1}{4}\left(\frac{1+\cos^2 2\theta_{hkl}}{\sin^2\theta_{hkl}\cos\theta_{hkl}}\right) \tag{3.3}$$

In most of the cases analyzed in this work we have assumed that the data presented in the experimental reports have been Lorentz-polarization corrected. In some cases we have not used the LP factor, because of the private communication of the authors or the quality of the fits. We have also chosen to neglect other corrections such as an absorption coefficient, the multiple scattering effect etc. Thus, the experimental intensities which will be compared with the modeled ones are obtained by dividing the raw experimental data by a correct LP factor and subtracting the background intensity:

$$I_{hkl}^{(exp)} = \frac{I_{hkl}^{(raw)}}{LP(\theta_{hkl})} - I^{(bg)}(q_{hkl}) \tag{3.4}$$

When the experimental resolution is small, the background scattering can be easily extracted. In most of the cases presented in this paper, we have established the background intensity on the basis of experimental data, where the Bragg peaks usually sit on a well defined broad scattering pattern. In two cases the background intensity resembled the scattering pattern from the microemulsion with a characteristic broad maximum. In these cases it was fitted with the scattering intensity for a microemulsion system given by [60]:

$$I^{(bg)}(q) = \frac{I_0}{\left(1 - \frac{I_0}{I_{max}}\right)\left(\frac{q^2}{q_{max}^2} - 1\right)^2 + \frac{I_0}{I_{max}}} \tag{3.5}$$

where I_0 is the intensity for $q = 0$ and q_{max} is the scattering vector length for which the intensity attains maximum I_{max}.

When the raw experimental intensities are corrected accordingly to the details of the experimental setup and the background intensity is subtracted one can proceed with fitting the modeled intensities. The first step is to determine the peak spacing and the cubic cell parameter a. If more than one ascription of the *hkl* Miller indices was reasonable all of the possibilities have been checked via the following fitting procedure and the best fit has been chosen.

The model amplitudes for the TPS based cubic phases have been described in detail in the preceding chapter. Here, to fit the data we will use the simplified model which assumes a flat contrast density profile $\rho(\xi) = \rho_0$ for $|\xi| \leq L/2$ and $\rho(\xi) = 0$ for $|\xi| > L/2$, where L is the width of the layer decorating the base minimal surface and ξ is a coordinate along the direction normal to the surface. Also the fluctuations of the layer will be neglected. Within this approximation the model scatering amplitude is:

$$A(\mathrm{q}, L) = F^S \frac{2\rho_0}{\alpha_{hkl} q} \sin\left(q\alpha_{hkl}\frac{L}{2}\right) \tag{3.6}$$

and since in comparison with experiment only the relative amplitudes matter, in order to simplify this expression, we can devide it by the factor $2a^3\rho_0$ which is constant for all hkl reflections. Finally the model scattering intensities are given by the following equation:

$$I_{hkl}^{(mod)}(L) = \mathcal{M}_{hkl}\left[F_{hkl}^{S\star}\frac{\sin\left(\alpha_{hkl}\,\pi\sqrt{h^2+k^2+l^2}\,L^\star\right)}{\alpha_{hkl}\,2\pi\sqrt{h^2+k^2+l^2}}\right]^2 \tag{3.7}$$

where $L^\star = L/a$ is the dimensionless layer width expressed in terms of the lattice constant a and all of the constants - the dimensionless structure factor $F^{S\star} = F^S/a^2$, multiplicity factor $\mathcal{M}_{hkl}$ and the correction parameters α_{hkl} are explicitly given in Tables 2-8 for the P, D, G, C(D), C(P), F-RD and I-WP based cubic phases.

Since the scattering intensity is measured in an arbitrary scale only the relative intensities of subsequent peaks can be determined. Thus in order to fit the experimental data, the model intensities have to be multiplied by a normalization constant Z which is chosen in such a way as to set the model intensity of one reference HKL peak to be exactly equal the experimental intensity.

$$Z = \left(\frac{I_{HKL}^{(exp)}}{I_{HKL}^{(mod)}} \right) \tag{3.8}$$

In all of the examples presented below we have chosen the first nonzero reflection as the reference peak. Then we checked whether any of the modeled structures satisfies the following relation:

$$I_{hkl}^{(exp)} \simeq Z I_{hkl}^{(mod)}(L^\star) \ \forall \ hkl \tag{3.9}$$

for any layer width L. The object to find the actual width of the layer decorating the minimal surface can be achieved by simply comparing the set of experimental intensities $I_{hkl}^{(exp)}$ with the modeled $I_{hkl}^{(mod)}(L^\star)$ ones for various layer widths. In practice it is numerically easier to look for the model scattering patterns best resembling the experimental ones when they are both expressed as continuous curves rather then a set of distinct values. The experimental and numerical intensity curves $I^{(exp/mod)}(q)$ have been reconstructed by a convolution of the set of $I_{hkl}^{(exp/mod)}$ values with the Gaussian resolution function $R(q) = \exp(-q^2/2\sigma_r^2)/(\sigma_r\sqrt{2\pi})$. The σ_r parameter is directly related to the half-widths $\delta I_{1/2}$ of the experimental peaks $\sigma_r \approx (1/2.3)\delta I_{1/2}$.

$$I^{(exp/mod)}(q) = \frac{1}{\sigma_r\sqrt{2\pi}} \sum_{hkl} \exp\left[\frac{-(q_{hkl} - q)^2}{2\,\sigma_r^2} \right] I_{hkl}^{(exp/mod)} \tag{3.10}$$

Thus instead of comparing the h, k, l peak intensities we have performed a minimization of the following integral:

$$\Delta(L^\star) = \int_0^\infty dq \left(I^{(exp)}(q) - Z I^{(mod)}(q, L^\star) \right)^2 \to min \tag{3.11}$$

with the variation parameter being the dimensionless layer width $L^\star$. Then the optimal layer width $L = aL^\star$ (for which $\Delta(L^\star)$ is minimal) has been assumed to be the real width of the layer decorating the base minimal surface.

Having established the width of the layer one can proceed with further analysis of the structure of the cubic phase. The following relation:

$$\phi = s_0^\star L^\star + \frac{\pi}{6}\chi L^{\star\,3} \tag{3.12}$$

yields the volume fraction ϕ of the layer ($s_0^\star = s_0/a^2$ is the dimensionless surface area of the base TPMS and χ is its Euler characteristic - both values are given in Table 1).

In order to tell whether a direct or inverse structure has been formed one can compare ϕ with the volume fractions of water (ϕ_w), surfactant (ϕ_s) and hydrocarbons (ϕ_h) in the system. A layer volume fraction ϕ comparable with the water volume fraction $\phi \approx \phi_w$ stands in favor of the direct phase - when the minimal surface is decorated with a water film. When ϕ is comparable with the joint volume fraction of surfactant and hydrocarbon $\phi \approx \phi_s + \phi_h$ more likely the inverse phase has been formed with the minimal surface draped with the surfactant bilayer. Still this method has a serious weakness. In many systems the cubic phases coexist with an excess water phase. Thus the system's composition does not reflect the composition of the cubic phase itself. Therefore a more reliable analysis is needed. It is based on the estimation of the surface area per surfactant head a_s as follows. The layer decorating the minimal surface is confined between two parallel surfaces laying at a distance $L/2$ away from the base minimal surface. The surface area per unit cell of these two interfaces is given by:

$$s_{\|}(L) = 2s_0^\star\, a^2 + \pi\chi L^2 \tag{3.13}$$

The parallel surfaces divide the volume into three regions: the layer and two disjoint continuous channels. In the case of the direct phase the hydrocarbon and surfactant molecules occupy the two channels. It's volume per unit cell is equal to $V_{dir} = (1-\phi)\, a^3$. When an inverse structure is formed the amphiphilic and hydrophobic molecules reside within the layer which's volume per unit cell is $V_{inv} = \phi\, a^3$. Knowing the molecular weight of the surfactant $M[g/mol]$, the densities of surfactant and hydrocarbon ($\rho_s[g/cm^3]$ and $\rho_h[g/cm^3]$ respectively) and the weight fractions of surfactant and hydrocarbon in the system (x_s and x_h) one can establish the number of surfactant molecules per cubic cell:

$$N_{dir/inv}(L) = V_{dir/inv}\,\frac{N_A}{M}\left(\frac{\rho_s}{1+\frac{x_h\rho_s}{x_s\rho_h}}\right) \times 10^{-24} \tag{3.14}$$

where $N_A = 6.023\times 10^{23}$ is the Avogadro constant and the factor 10^{-24} comes from the ratio of the cubic centimeter to cubic Angström ($1cm^3 = 10^{24}\text{Å}^3$). Finally the area per surfactant head:

$$a_{s\; dir/inv}(L) = \frac{s_{\|}(L)}{N_{dir/inv}(L)} \tag{3.15}$$

In this approach we assume that all of the hydrocarbons present in the system are confined within the surfactant bilayer or channel. In the case of a binary mixture the term in brackets in Eq.(3.14) simplifies to the surfactant density. The density of surfactant is in principle an unknown feature as it can vary from one ordered phase to another. Still, as it will be shown in the examples below, the dependence of the surface area per surfactant head on the layer width is strong enough to settle with an approximated density. In most cases, the plot of $a_{s\,dir}$ and $a_{s\,inv}$ against the layer volume fraction enables unambiguous determination of the type of the structure.

3.2 Analysis of the experimental spectra

3.2.1 The DLPE, DEPE and DOPE systems

The DEPE/water system [61]

The system is composed of 1,2-dielaidoyl-*sn*-glycero-3-phosphoethanolamine (DEPE) dispersion in an excess water phase. The diffraction pattern consists of 9 Bragg reflections. Their spacing ($\sqrt{2}$, $\sqrt{3}$, $\sqrt{4}$, $\sqrt{6}$, $\sqrt{8}$, $\sqrt{9}$, $\sqrt{10}$, $\sqrt{12}$, $\sqrt{14}$) indicate a $Pn\bar{3}m$ symmetry (No. 224 in the International Crystallography Tables). The most commonly encountered structure of this symmetry is the double diamond D surface based phase. This assumption proved to be correct. Minimizing the integral Eq.(3.11) yielded the layer width $L = 0.162a$. This value correspond to the layer volume fraction $\phi = 0.3$. The experimental scattering pattern together with the model fit is shown on Figure 28. In addition we have been able to identify the background scattering intensity as the scattering from the microemulsion (Eq.(3.5) with parameters $I_0 = 0.174 I_{110}$, $I_{max} = 0.714 I_{110}$ and $q_{max} = 0.15\text{Å}^{-}1$). This suggests that the cubic mono-crystalline regions are separated by volumes filled with disordered bicontinuous phase or microemulsion formed in the excess water phase.

The inset of Figure 28 shows the area per surfactant head as a function of the layer volume fraction ϕ. The molecular weight of DOPE is $M_{DOPE} = 744[g/mol]$. In our calculations we have assumed its density to be equal to unity ($\rho_{DOPE} = 1$). For $\phi \approx 0.3$ the area per head is $a_{s\,dir} \approx 50\text{Å}^2$ or $a_{s\,inv} \approx 120\text{Å}^2$. The comparison of these two values strongly supports the direct phase (dir) with a water film decorating the minimal surface.

Since the system is prepared with excess water, it is important to note here, that determining the layer width L and the structure type is a direct way of establishing the composition of the cubic phase.

The DLPE/α-tocopherol/water system [62]

The system under investigation contained a fully hydrated 1,2-dilauoryl-*sn*-glycero-3-phosphoethanolamine (DLPE) with an addition of 10mol% α-tocopherol. The experimental scattering spectrum consisted of 9 reflections $\sqrt{2}$, $\sqrt{3}$, $\sqrt{4}$, $\sqrt{6}$, $\sqrt{8}$, $\sqrt{9}$, $\sqrt{10}$, $\sqrt{12}$, $\sqrt{14}$ ($Pn\bar{3}m$ symmetry No. 224). The authors of [62] concluded that it is the double diamond D structure. It is partially right - Figure 29 shows the fit for the D structure ($\phi = 0.2$, $a_{s\,dir} \approx 45\text{Å}^2$ and $a_{s\,inv} \approx 180\text{Å}^2$ indicating a direct phase). Still the sole analysis of the peak positions overlooks the phase coexistence with the hexagonal phase. All of the peaks are fitted very well besides the 111, 221 and 222 reflections spaced 1, $\sqrt{3}$ and $\sqrt{4}$ respectively. The inset in the upper left corner of Figure 29 shows the modeled intensity subtracted from the experimental data. The remaining peaks are characteristic of a hexagonal

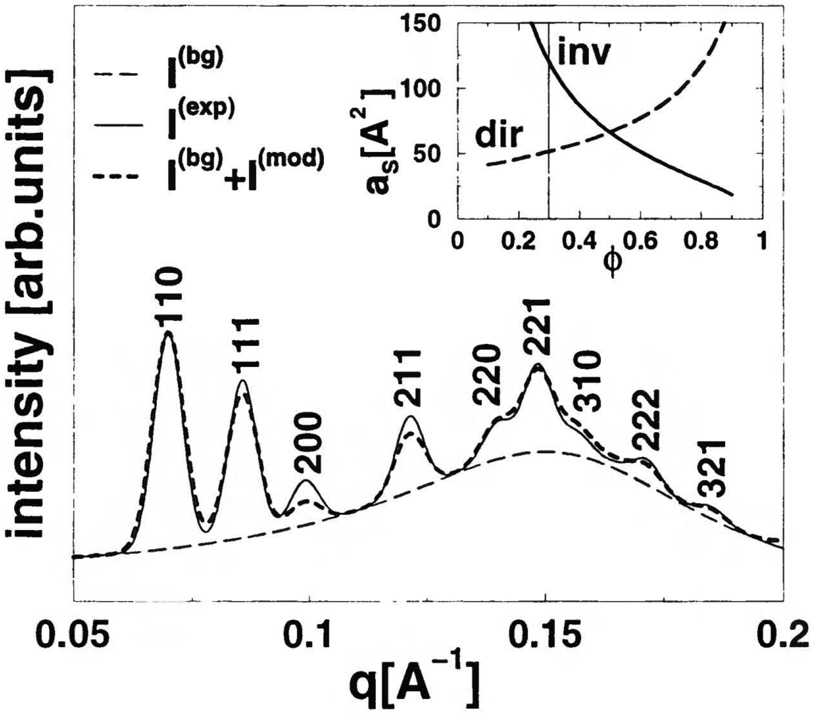

Figure 28: The fit of the experimental scattering pattern reported in [61]. The solid line shows the experimental intensity curve reproduced using Eq.(3.10). The thin dashed line gives the background intensity fitted through Eq.(3.5). The thick solid line presents the theoretical fit for the D based cubic phase of the layers volume fraction $\phi = 0.3$. The areas per lipid head for a direct and an inverse type of the D structure are drawn in the inset (dashed and solid lines respectively). For $\phi = 0.3$ the area per lipid is $a_{s\,dir} \approx 50\text{Å}^2$ for the direct phase and $a_{s\,inv} \approx 120\text{Å}^2$ for an inverse type. This indicates a D based direct cubic phase of the water film volume fraction $\phi = 0.3$.

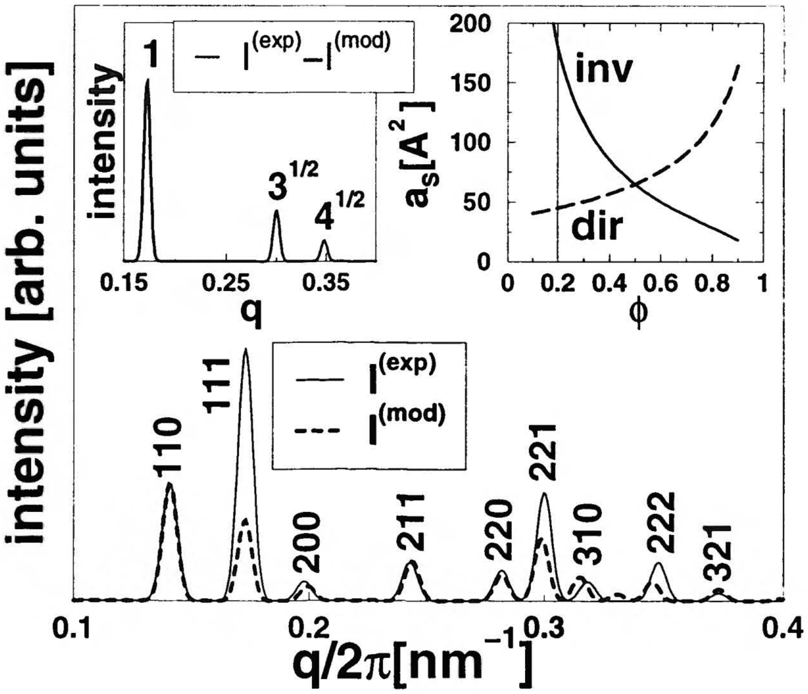

Figure 29: The fit of the experimental scattering pattern reported in [62]. The solid line shows the experimental scattering curve Eq.(3.10), while the thick dashed line gives the theoretical fit for a D based phase of the layer volume fraction $\phi = 0.2$. The very high intensity (in comparison with a fitted value) of the experimental 111, 221 and 222 peaks imply a coexistence with a hexagonal phase of a lattice parameter $a^{(hex)} = (2/3)a^{(D)}$. The intensity difference between the experimental and fitted curve is shown in the top left inset. The top right inset presents the areas per lipid head as a function of the layer volume fraction.

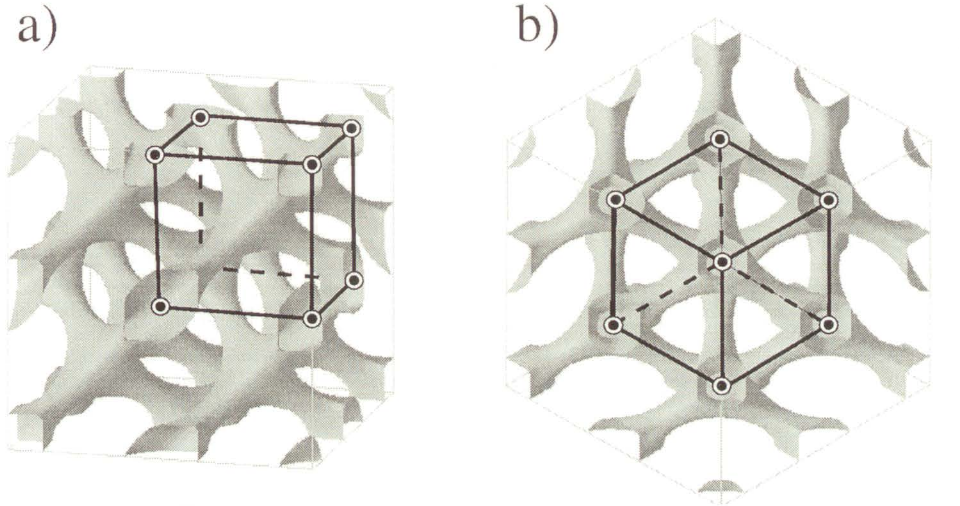

Figure 30: Visualization of the two disjoint channels forming the double-diamond periodic network. Part a) shows the cubic cell of a lattice parameter $a^{(D)}$ used for the scattering spectrum evaluation. It is given by black lines with the vertices marked with white-black circles. b) the same network of channels seen along the diagonal of the cubic cell. The edges of the cubic cell form a two dimensional hexagonal lattice of a parameter $a^{(hex)} = (\sqrt{2}/\sqrt{3})a^{(D)}$.

phase. A very similar phenomenon has been discovered in a 1,2-dioleoyl-*sn*-glycero-3-phosphocholine (DOPE) dispersion in water [63]. The reflections 10, 11 and 20 from the hexagonal phase were superimposed on the 111, 221 and 222 peaks originating from the double-diamond structure. What is particularly interesting is the ratio between the hexagonal and cubic cell parameters. The scattering vector length is related to the hexagonal lattice parameter by $q_{hk}^{(hex)} = (2\pi/a^{(hex)})(2/\sqrt{3})\sqrt{h^2+k^2-hk}$ and for the cubic lattice $q_{hkl}^{(D)} = (2\pi/a^{(D)})\sqrt{h^2+k^2+l^2}$. Since $q_{10}^{(hex)} = q_{111}^{(D)}$:

$$q_{10}^{(hex)} = \frac{2\pi}{a^{(hex)}}\frac{2}{\sqrt{3}} = \frac{2\pi}{a^{(D)}}\sqrt{3} = q_{111}^{(D)} \tag{3.16}$$

then $a^{(hex)} = (2/3)a^{(D)}$. The double-diamond structure consist of two separate continuous networks of rods connected four by four. If one looks at a projection of the node positions on a [111] plane perpendicular to the diagonal of the cubic cell he would see a 2D hexagonal lattice with the lattice parameter $a^{(hex)} = (\sqrt{2}/\sqrt{3})a^{(D)}$ (Figure 30). It is significantly different from the one established from the scattering data. Thus the ratio $a^{(hex)} = (2/3)a^{(D)}$ seen in two different systems can not be explained by a simple geometrical - epitaxial relationship. The relation between the lattice parameters could yield in principle interesting information on the elasticity constants of DLPE and DOPE monolayers.

The DOPE/water system [65]

A 50 weight % DOPE-water dispersion was studied in a wide temperature range (4°C< T < 80°C). At high temperatures the hexagonal phase dominate the scattering pattern. However for temperatures below T = 30°C several peaks of two coexisting cubic phases appear. The experimental scattering curve for T = 5°C is presented in Figure 31a with open triangles. The pattern consists of the $\sqrt{2}$, $\sqrt{3}$, $\sqrt{6}$ and $\sqrt{9}$ reflections originating from the $Pn\bar{3}m$ symmetry with a 132Å unit cell and $\sqrt{2}$, $\sqrt{4}$ and $\sqrt{6}$ peaks ($Im\bar{3}m$, 168Å).

We begin the analysis with a fit of the background intensity. Figure 31a shows $I^{(bg)}$ (Eq.(3.5) with parameters $I_0 = 0.8I_1$, $I_{max} = 4.7I_1$ and

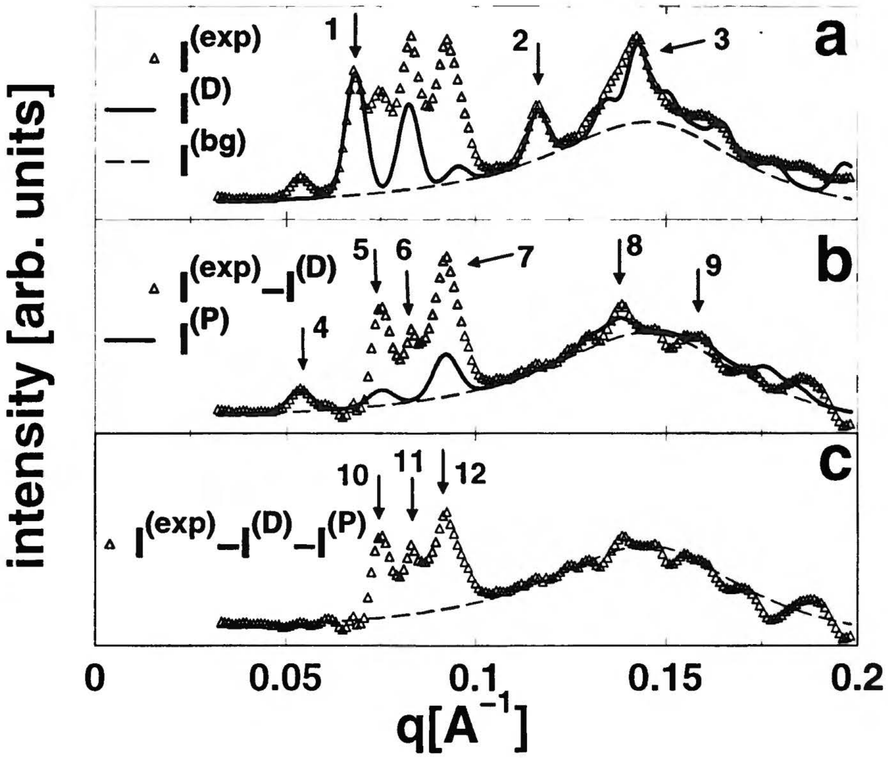

Figure 31: The experimental [65] intensity curve is shown with open triangles in the a) part of the figure. The fits for the background intensity (dashed line) and for the D phase ($\phi = 0.1$) (solid line) is shown. The arrows marked 1,2 and 3 point to the 110 (1), 211 (2) and a group of the 220, 221 and 310 peaks (3) which are reconstructed very accurately. Then the intensity of the D based phase is subtracted from the experimental curve. The remaining intensity curve is shown with open triangles in b). The solid line presents a theoretical intensity for a P based phase ($\phi = 0.1$). After subtracting the P intensity only three peaks remain at spacing frequency $\sqrt{4}$, $\sqrt{5}$ and $\sqrt{6}$ marked with the 10, 11 and 12 respectively.

$q_{max} = 0.145\text{Å}^{-}1$, where I_1 corresponds to the intensity of the first peak located at 0.0529Å). Next we assume that the $Pn\bar{3}m$ cubic phase is based on a double-diamond D TPMS. Minimization of the integral Eq.(3.11) yields a small volume fraction of the layer $\phi \in (0.1, 0.2)$. The fit is shown on Figure 31a with a solid line. The intensities of the 211 reflection (marked with an index 2 on the figure) and the group of the 220, 221 and 310 peaks (marked with 3) are reconstructed very accurately which supports the assumption on the structure type. The molecular weight of DOPE is $M_{DOPE} = 744[g/mol]$. Evaluating Eq.(3.15) we have obtained the following areas per surfactant head: $a_{s\,dir} \in (40.3, 44.4)$ Å^2 and $a_{s\,inv} \in (362.8, 177.7)$Å^2. The values for the direct phase are similar to the ones computed for the systems described above. This fact, together with a good fit of the intensities confirm a D direct structure. In the next step we subtract the modeled intensity for the D structure from the original experimental data. The remaining intensity contains 4 well resolved peaks of the spacing $\sqrt{2}$:$\sqrt{4}$:$\sqrt{5}$:$\sqrt{6}$ (on Figure 31b marked with the indices 4,5,6 and 7 respectively). If we assume that the $\sqrt{2}$:$\sqrt{4}$:$\sqrt{6}$ reflections originate from an $Im\bar{3}m$ cubic lattice, only the P based phase could be fitted to this data. It means that the sequence should be 110, 200 and 211 reflections. Minimizing Eq.(3.11) gives a small volume fraction of the layer. This is also supported by relatively large intensity of the 222, 321 reflections fitting the experimental peak marked by the index 8 on the figure and 400, 411 (mark 9). Moreover in the $\phi \in (0.1, 0.2)$ range of volume fractions the area per surfactant head for the direct phase assume reasonable values $a_{s\,dir} \in (38.1, 42.2)$Å^2. Thus if the assumption that the P structure has been formed is correct, most probably it would be a direct phase with a small volume fraction of the water film, the same as for the coexisting D structure.

After subtracting the intensity for the P structure the remaining intensity curve consists of three peaks $\sqrt{4}$:$\sqrt{5}$:$\sqrt{6}$ (Figure 31c, marks 10, 11 and 12 respectively). A very similar pattern has been reported for a sodium dodecyl sulfate (SDS)/ hydrocarbon / water system [66] where it has been assigned to a $Pm\bar{3}n$ micellar cubic phase. The peaks could also be interpreted as an evidence of some unidentified third phase separating the monocrystalline regions of D and P phases. As we have the data for only one temperature it is impossible to risk any final judgment. A similar analysis of the scattering patterns during the whole temperature scan would probably give reliable answers. For example one could track the kinetics of the phase transition. Assuming that the D and P structure assignment is correct, one can extract approximate volume fractions of these phases. Namely, amplitude of the 000 reflection is proportional to the volume occupied by the layer decorating the minimal surface (see Eqn(2.6) in chapter 2):

$$I_{000}(L) \propto [\phi(L)V]^2 \tag{3.17}$$

where V is the volume of the given cubic phase. When the experimental scattering pattern has been fitted with modeled intensities for a given layer width L, the intensity of the 000 reflection can be extracted from the following relation:

$$I_{000} = I_{000}^{(mod)}(L)\frac{I_{hkl}^{(exp)}}{I_{hkl}^{(mod)}(L)} \tag{3.18}$$

thus the volume ratio of the D and P phase is:

$$\frac{V^{(D)}}{V^{(P)}} = \sqrt{\frac{I_{000}^{(D)}}{I_{000}^{(P)}}\left(\frac{\phi^{(P)}}{\phi^{(D)}}\right)} \tag{3.19}$$

Substituting the values of $\phi^{(D)} = \phi^{(P)} = 0.15$, $I_{110}^{(D\,exp)} = 84$ [arb. units], $I_{110}^{(P\,exp)} = 17$ [arb. units], $I_{110}^{(D\,mod)}(L(\phi = 0.15)) = 2.638$, $I_{110}^{(P\,mod)}(L(\phi = 0.15)) = 2.364$, $I_{000}^{(D\,mod)} = 3.690$ and $I_{000}^{(P\,mod)} = 5.502$ we obtain:

$$\frac{V^{(D)}}{V^{(P)}} \approx 1.7 \tag{3.20}$$

a value that would be very difficult to determine without the analysis of the peak intensities. Furthermore having this kind of data for a whole range of the temperature scan one could determine the phase transition speed. Which together with information on the third metastable phase could lead to a better understanding of the phase transition mechanisms.

3.2.2 The GMO systems

The GMO/Polaxamer 407/water system [67]

In ref. [67] a study of a glycerolmonooleate (GMO) with an addition of a $PEO_{98}PPO_{67}PEO_{98}$ (Polaxamer 407) polymer mixture in an excess water is presented. We have been able to extract data of two scattering patterns - one for a 4 weight % polymer to GMO ratio (Figure 32a) and the second for a 7.4 wt % ratio (Figure 32b). The first system has been successfully fitted with a D based structure of the layer volume fraction $\phi = 0.45$. Too small value of the 200 fitted intensity in comparison to the measured one could be explained

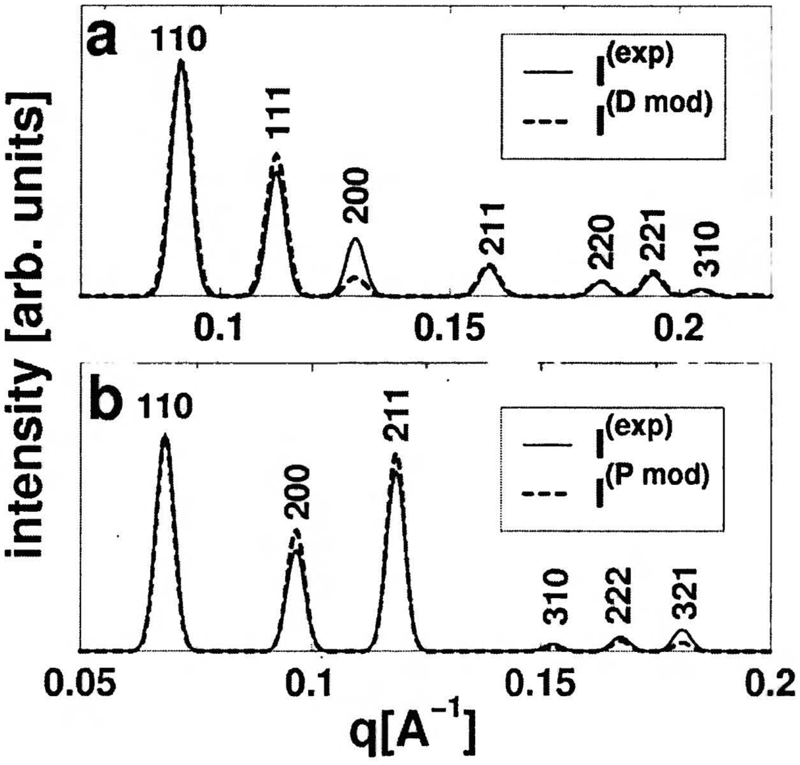

Figure 32: The scattering patterns reported in [67 (solid lines) together with the theoretical fits (dashed lines) a) a D based phase ($\phi = 0.45$), b) a P based phase ($\phi = 0.5$).

by a small addition of the hexagonal phase which in fact has been reported in this system [67]. The superposition of the 10 peak originating from the hexagonal phase on the 200 Bragg reflection of the double-diamond D based phase is yet another confirmation of the epitaxial relationship described above for the DLPE [62] and DOPE [63] systems. The areas per surfactant head for $\phi = 0.45$ are $a_{s\,dir} = 39\text{Å}^2$ for a direct phase and $a_{s\,inv} = 48\text{Å}^2$ for an inverse structure. The value of 39Å^2, as compared to the existing literature, seems more reasonable and thus we propose a D direct phase for this system.

The second scattering pattern has been fitted with the intensities of the P based structure: $\phi = 0.5$, $a_{s\,dir} = a_{s\,inv} = 36.7\text{Å}^2$. In this case we cannot distinguish the direct from the inverse structures.

The GMO/Polaxamer 407/water system [53]

As in the last example, the system under investigation is the GMO/Polaxamer 407/water mixture. Reference [53] presents a thorough examination of its phase behavior. Besides the hexagonal and lamellar structures, Landh shows [53] several scattering patterns from the cubic phase region in the phase diagram.

Four of the experimental patterns together with our fits are shown in Figure 33(a-d). In the case of all of the presented patterns the modeled intensities fitted the experimental scattering curves quite well. The data for all these fits is included in Table 9. To enhance the analysis of the structure type we made an attempt to compare the fitted volume fraction ϕ of the layer decorating the TPMS with the joined volume fraction $\phi_{GMO+P407}$ of surfactant and polymer in the system. For the mixture of composition $(c_{GMO}/c_{P407}/c_{water})$ wg % we have:

$$\phi_{GMO+P407} = \frac{\frac{x_{GMO}}{\rho_{GMO}} + \frac{x_{P407}}{\rho_{P407}}}{\frac{x_{GMO}}{\rho_{GMO}} + \frac{x_{P407}}{\rho_{P407}} + \frac{x_{water}}{\rho_{water}}} \tag{3.21}$$

where $x_i = c_i/100$ are the weight fractions.

For the first three systems both the fitted volume fractions ϕ of the layer

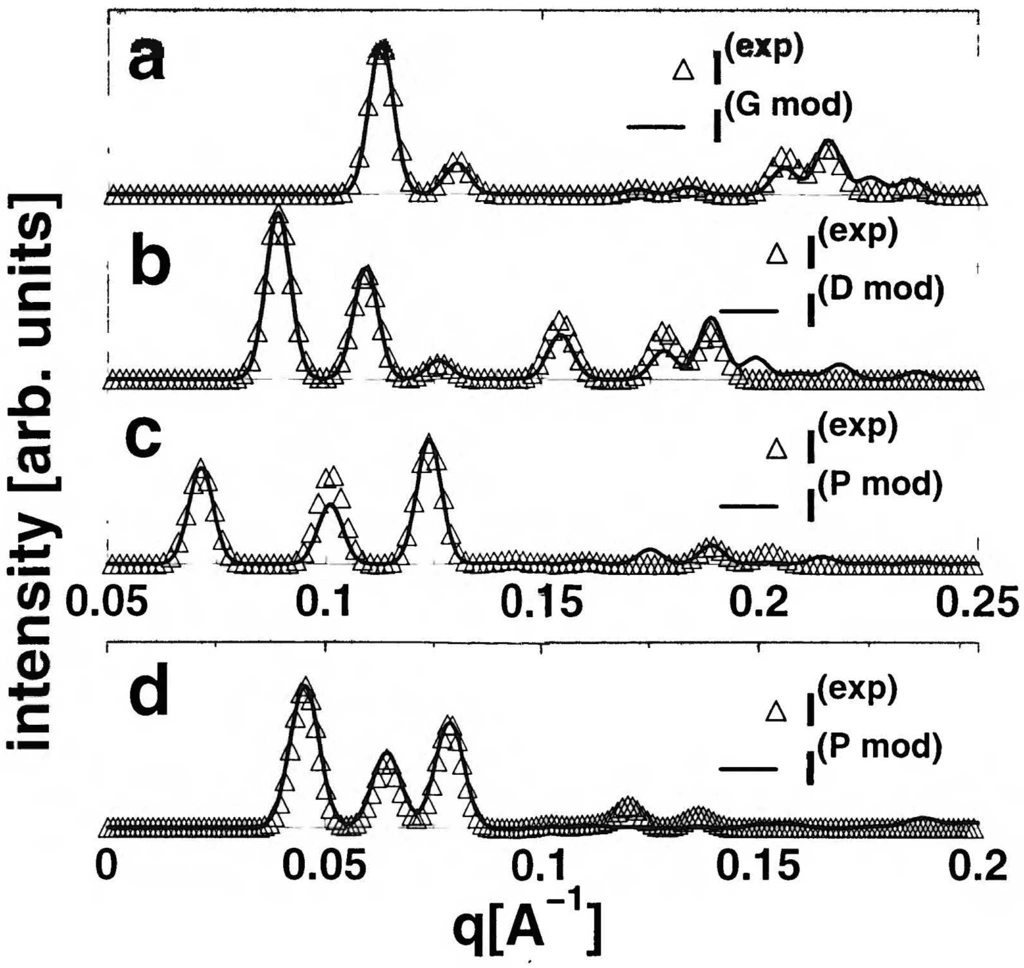

Figure 33: Successful fits of four scattering patterns reported in [53]. The experimental patterns are drawn with open triangles and theoretical fits with solid lines. a) a G gyroid cubic phase, b) a D double diamond cubic phase, c) and d) two P based cubic phases.

Analysis of the GMO/P407/water systems [53]									
comp. wg % $c_{GMO}/c_{P407}/c_w$	fitted TPS	a[Å]	fitted ϕ	$\phi_{ch} = 1 - \phi$	$\phi_{GMO+P407}$ (Eq.(3.21))	a_s[Å^2] DIR	a_s[Å^2] INV	prop. type	prop. type [53]
68.6/2/29.4	G	136.6	0.25	0.75	0.718	38	114	DIR	INV
63.1/1/35.9	D	99.7	0.3	0.7	0.654	34	79.3	DIR	INV
60.1/5.1/34.8	P	124.3	0.4	0.6	0.664	39	58.4	DIR	INV
38.7/14.1/47.2	P	195.6	0.55	0.45	0.538	37.3	30.5	?	INV

Table 9: First column - weight fractions of the explored mixtures. Second column - the base TPMS. The fits are presented graphically on Figure 33. The following columns contain the lattice parameter a, the volume fraction of the layer (ϕ) and the volume fraction of the two disjoint channels ($\phi_{ch} = 1 - \phi$). This two values should be compared with the joined volume fractions of the surfactant and polymer (sixth column). In the first three cases the $\phi_{GMO+P407}$ values are similar to the volume fractions of the channels which indicate a direct type of the cubic phase. Small differences (up to $\sim 10\%$) may be caused by the fact that the fits determine the width of the layer of an effective contrast which might be slightly different then the actual layer width including the surfactant heads. Another possible explanation is that the system is a multi phase one with additional regions of microemulsion, sponge phase or excess water. The seventh and eight column present the computed surface areas per surfactant head for a direct and inverse structures for the layer volume fraction given in column four. The last two columns show our determination of the structure type compared with the one presented in ref. [53].

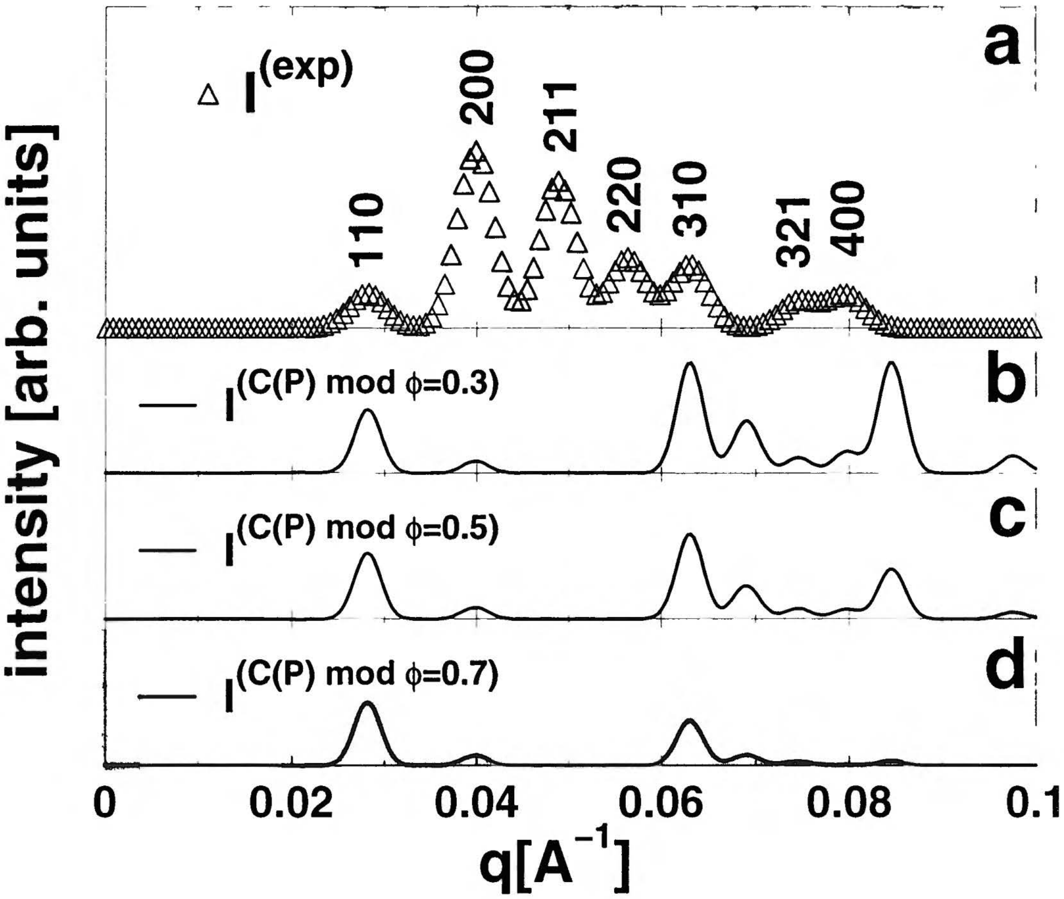

Figure 34: Experimental scattering curve from ref.[53] is shown with open triangles. Its ascription to a C(P) based phase was wrong as it is seen from comparison with three theoretical patterns for this structure for $\phi = 0.3$, $\phi = 0.5$ and $\phi = 0.7$ (b, c, d respectively).

compared with the joined volume fraction $\phi_{GMO+P407}$ of surfactant and polymer and the surface areas per surfactant head point out to the direct structures. The data is convincing enough to risk a statement that ascribing these patterns to inverse phases in ref. [53] was wrong. In the case of the fourth system it is impossible to decide which type of the P structure has formed. The fitted volume fraction ϕ suggests an inverse phase, but the area per surfactant head is more reasonable for the direct structure. As was noted in [53] on increasing the water weight fraction the system underwent a phase transition. Thus a transition from a direct to an inverse phase could be possible. For even higher water weight fraction ($c_{water} > 50$) Landh has recorded a diffraction pattern, interpreted as an evidence of the appearance of the C(P) based cubic phase. A typical pattern from this region (34.18/14.77/51.05) is shown in Figure 34a. In [53] it was suggested that the $1{:}\sqrt{2}{:}\sqrt{3}{:}\sqrt{4}{:}\sqrt{5}{:}\sqrt{7}{:}\sqrt{8}$ reflections originate from a C(P) structure with a lattice parameter $a = 315.3$Å. However we could not fit the experimental pattern with the C(P)'s spectrum for any layer width ϕ. To illustrate how different the C(P)'s patterns are, we have showed the $I^{(C(P)\,mod)}$ (Eqn. 3.10) for $\phi = 0.3$, 0.5 and 0.7 (Figure 94b-d). Thus we suggest that it is not a C(P) based phase being rather a P based phase coexisting with some unknown phase.

3.2.3 The DDAB/cyclohexane/water system [6]

The system composed of Didodecyl Dimethyl Ammonium Bromide (DDAB), cyclohexane and water. We have been able to extract the scattering intensity from two scattering patterns. The first one of a composition (52.9/13.2/33.9) wg % of DDAB/C_6H_{12}/H_2O. The experimental scattering pattern together with the model fit for a double-diamond D based phase is shown in Figure 35. The best fit was obtained for $\phi = 0.4$. For this ϕ value the areas per surfactant head (for $\rho_{DDAB} = 1[g/cm^3]$, $\rho_{C_6H_{12}} = 0.78[g/cm^3]$ and $a = 120$Å) are $a_{s\,dir} = 43$Å^2 for a direct phase and $a_{s\,inv} = 64.6$Å^2 for an inverse one. The second value is similar to that proposed by Barois $a_s = 68$Å^2 [6]. It is also in good agreement with an expected chain length of the DDAB molecule. The molecular weight of DDAB is $M_{DDAB} = 462[g/mol]$, thus, for $a_s \approx 65$Å^2, it's length is: $l_s = V_{DDAB}/a_s = M_{DDAB}/(0.6023\rho_{DDAB}) \approx 12$Å. Furthermore for the lattice parameter $a = 120$Å and for the layers volume fraction $\phi = 0.4$ the corresponding layer width $L = 0.22a = 26.4$Å. Thus the layer width is approximately twice as large as the length of the surfactant molecule ($L \approx 2l_s$). All this evidence stands in favor of an inverse structure.

The second scattering pattern has been recorded for a mixture of composition (41.7/9.3/49) wg % of DDAB/C_6H_{12}/H_2O respectively. The experimental scattering curve is shown on Figure 36. The authors of [6] suggested that this pattern originates from a P based structure. Indeed, we obtained the best fit for the P structure with $\phi = 0.45$. The 110, 211, 321 peaks are reconstructed very accurately. The 222 and 411 reflections have acceptable values. The area per surfactant for a direct phase $a_{s\,dir} = 62.3$Å^2 confirms the choice of a P direct structure. However the intensities of the 200 and 400 experimental peaks are by far greater then the modeled ones. After subtraction of the modeled intensities from the experimental pattern we have obtained a pattern typical for a lamellar structure (see inset in the right top

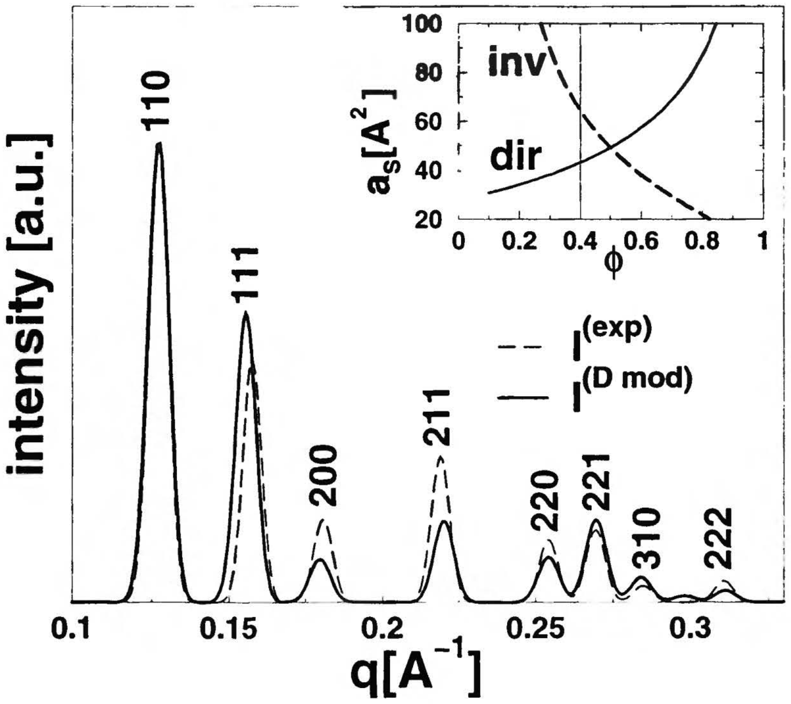

Figure 35: A fit for a DDAB/cyclohexane/water system described in [6]. The experimental intensity is shown with a dashed line while solid line presents theoretical pattern for a D TPMS based cubic phase with the layer volume fraction $\phi = 0.4$. Although the fit is not perfect, the value of the area per surfactant head for an inverse phase $(a_{s\ inv}(\phi = 0.4) = 64.6\text{Å}^2$ confirms the choice of the structure and layer width. The areas per DDAB per molecule for a direct (solid line) and inverse (dashed line) structures are shown in the inset.

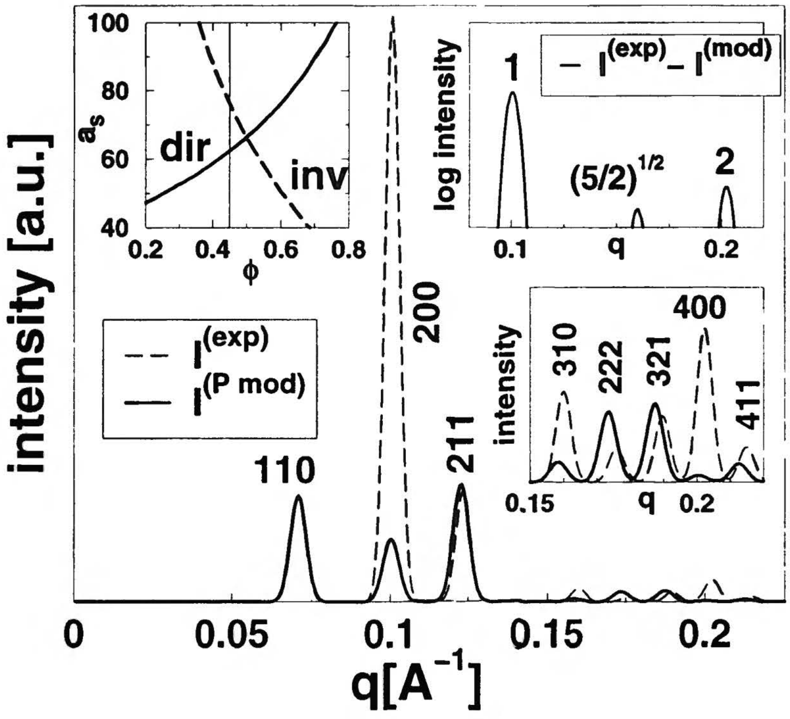

Figure 36: The experimental scattering intensity reported in [6] is shown with a dashed line in the main figure and the lower right inset. The best fit with theoretical spectra was obtained for a P based structure for $\phi = 0.45$ (solid line). The 110, 211, 222, 321 and 411 reflections are reconstructed quite well. The areas per surfactant head for a direct (solid line) and inverse type (dashed line) of the P structure are drawn in the top left inset. The top right one show the difference between the experimental intensity and the fitted pattern for a P structure. The remaining peaks spaced at the ratio 1:2 are characteristic of a lamellar phase indicating a phase coexistence. The $\sqrt{5/2}$ peak might originate at some transition state.

corner of Figure 36). From the peak positions one can deduce the lamellar repeat distance d to cubic lattice parameter a ratio: $d/a = 1/2$. Thus we conclude that the investigated mixture was in fact a two phase region. Furthermore the epitaxial relationship between the lattice parameters of the cubic and lamellar phase suggests a phase transition mechanism illustrated on Figure 37.

Namely, when crossing the phase boundary from the lamellar region to the P region the number of passages drastically increase. At some point the passages order in the 2D lamellar planes in a square lattice to form a P based cubic structure.

3.2.4 Polimerized G structure [68]

We would also like to present a fit to the experimental pattern of a polimerized G structure. The system described in [68] was an aqueous solution of a cetyltrimethylammonium chloride (CTAC) with an addition of tetraethylorthosilicate (TEOS). After reaching equilibrium the system was left for several hours in order to let the hydrolysis of TEOS takes place. Next the mesoporous solids obtained in the polimerization reaction were analyzed. Figure 38 shows the experimental scattering pattern of the mesoporous material of the $Ia\overline{3}d$ symmetry. This spectrum was successfully fitted with the scattering intensities for a G based structure of the layer volume fraction $\phi = 0.45$. The corresponding layer width is $L = 0.149a = 14.6$Å. Thus fitting the scattering pattern can also be a method for an efficient layer width measurement. The visualization of this mesoporous structure is presented in

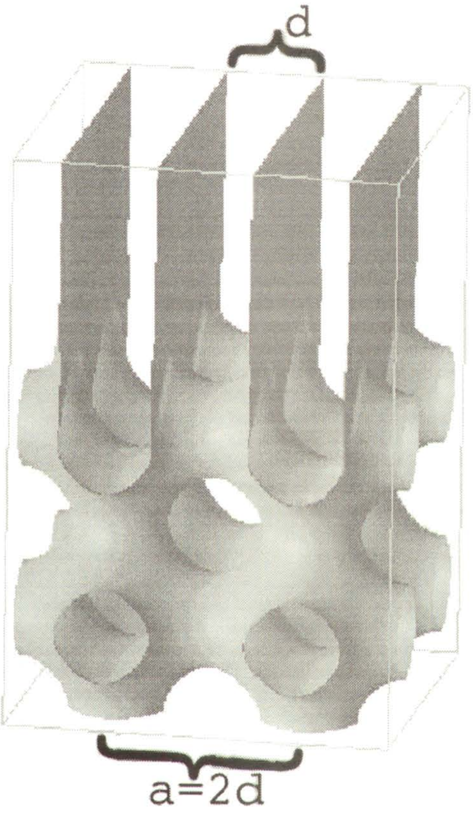

Figure 37: Schematic illustration of the lamellar to P TPMS based cubic phase transition and coexistence. The ratio between the cubic lattice constant a and the lamellar repeat distance d is indicated by the x-ray spectra [6].

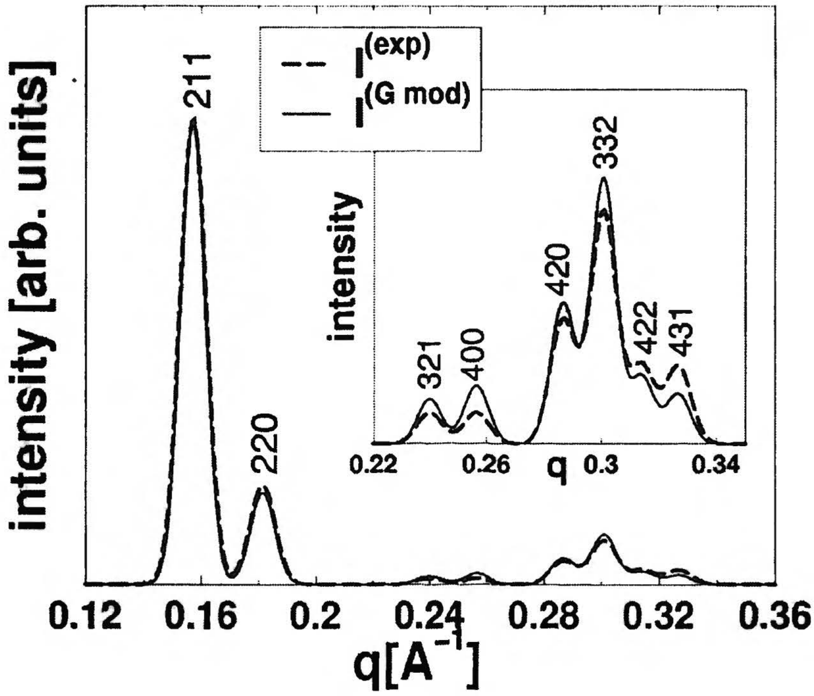

Figure 38: Comparison of the experimental [68] scattering pattern of a polimerized mesoporous material of an $Ia\bar{3}d$ symmetry (dashed line) with a theoretical spectrum for a gyroid G TPMS based phase of a layer volume fraction $\phi = 0.45$ (solid line).

Figure 39.

3.2.5 The $R_6^F\Sigma EO_2$/water system [9]

This last example is meant to show that the analysis of the intensity of the Bragg reflections can be done without performing the fitting procedure given by Eq.(3.11). It can be done when the intensities of several allowed peaks

Figure 39: A computer visualization of the G gyroid TPS based cubic phase determined by fitting the experimental SAXS pattern (Figure 38). The darker areas correspond to the subvolume ($\phi = 0.45$) occupied by the polimerized bilayer.

are very small. In the preliminary analysis it is enough to draw the relative intensity of the strongest reflections in respect to one reference peak as a function of the layer width L:

$$I_{hkl}(L)[I_{HKL}] = \frac{I^{(mod)}_{hkl}(L)}{I^{(mod)}_{HKL}(L)} \tag{3.22}$$

The reference peak should have a large intensity and possibly the smallest HKL indices. In the case of all three simple structures P, D and G the first reflection is a good candidate. Figure 40 shows the intensities of the strongest reflections of the D based phase in terms of the reference peak $HKL = 110$. These in turn can be compared with analogously expressed

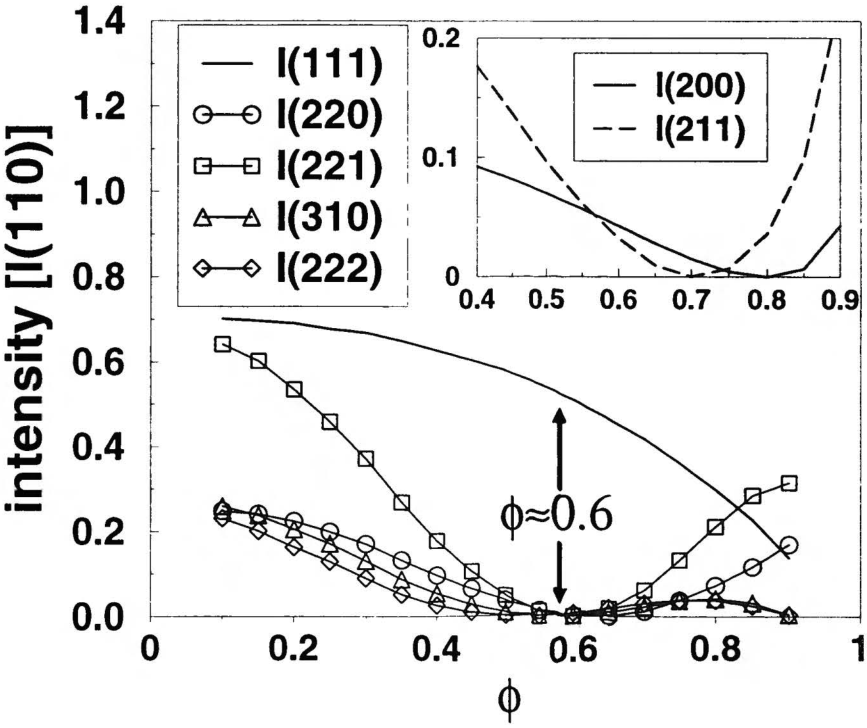

Figure 40: The theoretical intensities for the D TPMS based phase of the 111 (solid line), 220 (circles), 221 (squares), 310 (triangles) and 222 (diamonds) reflections expressed in terms of the intensity of the 110 peak. the arrows mark the layer volume fraction $\phi \approx 0.6$ for which the theoretical intensities are in accordance with experimental measurements [9]. The 111 intensity has been measured to be $I_{111} \approx 0.5 I_{110}$ while the 220, 221, 310 and 222 peaks were very weak ($< 0.01 I_{110}$). The inset show the theoretical intensities of the 200 and 211 reflection, experimentally measured to be $I_{200} \approx 0.01$ and $I_{211} \approx 0.03$.

spacing	*hkl* assignment	$I^{(exp)}$
$\sqrt{2}$	110	1
$\sqrt{3}$	111	~ 0.5
$\sqrt{4}$	200	~ 0.01
$\sqrt{6}$	211	~ 0.03
$\sqrt{8}$	220	< 0.01
$\sqrt{9}$	221	< 0.01
$\sqrt{10}$	310	0
$\sqrt{12}$	222	0

Table 10: The experimental intensities reported in [9]. The first column contains the spacing of the observed peaks, the second the *hkl* assignment and the last column contains the intensities expressed in terms of the intensity of the first (110) reflection.

intensities of the experimental scattering pattern of the fluorinated surfactant $C_6F_{13}C_2H_4SC_2H_4(OC_2H_4)_2OH$ ($R_6^F\Sigma EO_2$)/ water system reported in [9]. The experimental intensities are presented in Table 10. The intensity of 111 peak $I_{111}^{(exp)} \sim 0.5$, the small values of the 200, 211, 220, 221 reflections and absence of the 310 and 222 reflection are in good agreement with the theoretical values for the layer volume fraction $\phi \approx 0.6$. Furthermore at this value of ϕ the 200 and 211 reflections are significantly greater then zero, which is in accordance with the experimental measurement. It is important to note here that the intensity of the 200 reflection might be in fact bigger than the intensity of the 211 peak as expected by the theory. Due to rather small resolution of the scattering patterns presented in [9] the 200 peak lays within the vicinity of the broad 111 reflection. Thus it's intensity is probably underestimated.

4 Summary

The results of this work are summarized in chapter 2 by Eqs(2.2, 2.5) and Tables 2-8. The first equation enables reconstruction of the scattering amplitudes for any electron density profile and fluctuations. A detailed cross sectional density profile can be constructed from the knowledge of the microscopic details of the molecules present in the system. Then it can be tested by comparing the amplitudes evaluated through Eqn(2.2) with high quality experimental diffraction data.

For a simpler and faster analysis we propose modeling described by Eqn(2.5). It takes into account only the crude (Eqn(2.11)) electron density contrast and neglects the fluctuations. The last point has been justified in chapter 2.3. The Heaviside distribution form of the density function is related to the fact that the main contrast in most amphiphilic systems results from the electron density difference of water and hydrocarbons.

In the third chapter this simple method for a quantitative analysis of the scattering patterns of self assembled cubic phases has been applied to several experimental amphiphilic systems. Presented examples prove the utility of our method. Even such a crude model provides crucial information on the type of the structure, its microscopic details and on the stability of the system. Namely in phase coexisting systems one can determine the phases present, their structural relationships, volume ratios, etc. In time resolved techniques this could lead into an interesting insight on the kinetics and mechanisms of phase transitions.

Furthermore this approach could be used to study how the amplitude signs change with the parameters for more detailed density profiles. In this respect our approach could be used together with the method presented in [38] in order to find simple formulas for the intensity and density distribution in surfactant systems leading to reconstruction of the actual density map of the cubic phases in amphiphilic systems. We believe that our method will deepen the knowledge of these fascinating systems.

5 Appendices

5.1 Appendix 1: Nodal approximations for the C(P), C(D), F-RD and I-WP surfaces

The nodal approximations for the unit cells ($x, y, z \in (0,1)$) of the latter minimal surfaces are given by the equations below [40]:

$$C(P): \quad \cos(X) + \cos(Y) + \cos(Z) + 3\cos(X)\cos(Y)\cos(Z) = 0 \tag{5.1}$$

$$\begin{aligned} C(D): \quad & \cos(3X)\cos(Y)\cos(Z) + \cos(3Y)\cos(Z)\cos(X) \\ & + \cos(3Z)\cos(X)\cos(Y) + \cos(3X)\sin(Y)\sin(Z) \\ & + \cos(3Y)\sin(Z)\sin(X) + \cos(3Z)\sin(X)\sin(Y) \\ & - \sin(3X)\cos(Y)\sin(Z) - \sin(3Y)\cos(Z)\sin(X) \\ & - \sin(3Z)\cos(X)\sin(Y) - \sin(3X)\sin(Y)\cos(Z) \\ & - \sin(3Y)\sin(Z)\cos(X) - \sin(3Z)\sin(X)\cos(Y) = 0 \end{aligned} \tag{5.2}$$

$$\begin{aligned} F-RD: \quad & 12\cos(X)\cos(Y)\cos(Z) - 3\cos(2X)\cos(2Y) \\ & -3\cos(2Y)\cos(2Z) - 3\cos(2Z)\cos(2X) = 0 \end{aligned} \tag{5.3}$$

$$\begin{aligned} I-WP: \quad & 2\cos(X)\cos(Y) + 2\cos(Y)\cos(Z) + 2\cos(Z)\cos(X) \\ & - \cos(2X) - \cos(2Y) - \cos(2Z) = 0 \end{aligned} \tag{5.4}$$

where $X = 2\pi x$, $Y = 2\pi y$ and $Z = 2\pi z$ for the C(P), F-RD and I-WP surfaces and $X = \pi x$, $Y = \pi y$ and $Z = \pi z$ for the C(D) surface.

5.2 Appendix 2: Derivation of the Debye-Waller factor

The right side of the equation (2.26):

$$A(\mathrm{q}, \rho(\xi), \sigma) = F^S \frac{2}{\sigma\sqrt{2\pi}} \int_0^\infty d\xi \int_{-\infty}^{\infty} d\xi' \, \rho(\xi') \exp\left[\frac{-(\xi-\xi')^2}{2\sigma^2}\right] \cos(\alpha_{hkl} \, q \, \xi) \tag{5.5}$$

can be rewritten in the following form:

$$2F^S \int_{-\infty}^{\infty} d\xi' \rho(\xi') \frac{1}{\sigma\sqrt{2\pi}} \int_0^\infty d\xi \exp\left[\frac{-(\xi-\xi')^2}{2\sigma^2}\right] \cos(\alpha_{hkl} q \xi) \tag{5.6}$$

after substituting $x = \xi - \xi'$ we obtain:

$$\frac{2F^S}{\sigma\sqrt{2\pi}} \int_{-\infty}^{\infty} d\xi' \rho(\xi') \int_{-\xi'}^{\infty} dx \exp\left[\frac{-x^2}{2\sigma^2}\right] \cos(\alpha_{hkl} q (x + \xi')) \tag{5.7}$$

then, from the relation $\cos(a+b) = \cos(a)\cos(b) - \sin(a)\sin(b)$, we have:

$$\begin{aligned} &\frac{2F^S}{\sigma\sqrt{2\pi}} \int_{-\infty}^{\infty} d\xi' \rho(\xi') \cos(\alpha_{hkl} q \xi') \int_{-\xi'}^{\infty} dx \exp\left[\frac{-x^2}{2\sigma^2}\right] \cos(\alpha_{hkl} q x) - \\ &- \frac{2F^S}{\sigma\sqrt{2\pi}} \int_{-\infty}^{\infty} d\xi' \rho(\xi') \sin(\alpha_{hkl} q \xi') \int_{-\xi'}^{\infty} dx \exp\left[\frac{-x^2}{2\sigma^2}\right] \sin(\alpha_{hkl} q x) \end{aligned} \tag{5.8}$$

and after breaking up each of the integrals over x into a sum of two integrals $\left(\int_{-\xi'}^{\infty} dx = \int_{-\xi'}^{0} dx + \int_0^\infty dx\right)$ we obtain four integrals, that is:

$$A(\mathrm{q}, \rho(\xi), \sigma) = C_1 + C_2 - C_3 - C_4 \tag{5.9}$$

where

$$C_1 = \frac{2F^S}{\sigma\sqrt{2\pi}} \int_{-\infty}^{\infty} d\xi' \rho(\xi') \cos(\alpha_{hkl} q \xi') \int_{-\xi'}^{0} dx \exp\left[\frac{-x^2}{2\sigma^2}\right] \cos(\alpha_{hkl} q x) \tag{5.10}$$

$$C_2 = \frac{2F^S}{\sigma\sqrt{2\pi}} \int_{-\infty}^{\infty} d\xi' \rho(\xi') \cos(\alpha_{hkl} q \xi') \int_{0}^{\infty} dx \exp\left[\frac{-x^2}{2\sigma^2}\right] \cos(\alpha_{hkl} q x) \tag{5.11}$$

$$C_3 = \frac{2F^S}{\sigma\sqrt{2\pi}} \int_{-\infty}^{\infty} d\xi' \rho(\xi') \sin(\alpha_{hkl} q \xi') \int_{-\xi'}^{0} dx \exp\left[\frac{-x^2}{2\sigma^2}\right] \sin(\alpha_{hkl} q x) \quad (5.12)$$

$$C_4 = \frac{2F^S}{\sigma\sqrt{2\pi}} \int_{-\infty}^{\infty} d\xi' \rho(\xi') \sin(\alpha_{hkl} q \xi') \int_{0}^{\infty} dx \exp\left[\frac{-x^2}{2\sigma^2}\right] \sin(\alpha_{hkl} q x) \quad (5.13)$$

We will now rewrite the C_1 in the following form:

$$C_1 = \frac{2F^S}{\sigma\sqrt{2\pi}} \int_{-\infty}^{\infty} d\xi' \rho(\xi') \cos(\alpha_{hkl} q \xi') f_1(\xi') \quad (5.14)$$

where

$$f_1(\xi') = \int_{-\xi'}^{0} dx \exp\left[\frac{-x^2}{2\sigma^2}\right] \cos(\alpha_{hkl} q x) \quad (5.15)$$

is an asymmetrical function of ξ' because after a substitution $y = -x$ and since $\cos(-y) = \cos(y)$ we have:

$$f_1(\xi') = -\int_{\xi'}^{0} dy \exp\left[\frac{-y^2}{2\sigma^2}\right] \cos(\alpha_{hkl} q y) = -f_1(-\xi') \quad (5.16)$$

thus, since $\rho(\xi')$ and $\cos(\alpha_{hkl} q \xi')$ are symmetrical in ξ' the integral C_1 is equal to zero. Similar argument applies to C_3:

$$C_3 = \frac{2F^S}{\sigma\sqrt{2\pi}} \int_{-\infty}^{\infty} d\xi' \rho(\xi') \sin(\alpha_{hkl} q \xi') f_3(\xi') \quad (5.17)$$

where

$$f_3(\xi') = \int_{-\xi'}^{0} dx \exp\left[\frac{-x^2}{2\sigma^2}\right] \sin(\alpha_{hkl} q x) \quad (5.18)$$

is symmetrical because ($y = -x$; $\sin(-y) = -\sin(y)$):

$$f_3(\xi') = \int_{\xi'}^{0} dy \exp\left[\frac{-y^2}{2\sigma^2}\right] \sin(\alpha_{hkl} q y) = f_3(-\xi') \quad (5.19)$$

Again two of the functions under the integral over ξ' are symmetrical ($\rho(\xi')$ and $f_3(\xi')$) and one is asymmetrical ($\sin(\alpha_{hkl} q \xi')$) and $C_3 = 0$. The integral over x in C_4 is independent of ξ' and since $\sin(\alpha_{hkl}q\xi')$ is asymmetrical, C_4 is also equal to zero. Thus the only possibly nonzero component is C_2. Since both $\cos(\alpha_{hkl}qx)$ and $\exp[-x^2/2\sigma^2]$ are symmetrical in x the integral $\int_0^\infty dx = (1/2)\int_{-\infty}^\infty dx$ and:

$$C_2 = \frac{2F^S}{\sigma\sqrt{2\pi}}\int_{-\infty}^{\infty} d\xi'\rho(\xi')\cos(\alpha_{hkl}q\xi')\frac{1}{2}\int_{-\infty}^{\infty} dx\exp\left[\frac{-x^2}{2\sigma^2}\right]\cos(\alpha_{hkl}qx) \tag{5.20}$$

where

$$\frac{1}{2}\int_{-\infty}^{\infty} dx\exp\left[\frac{-x^2}{2\sigma^2}\right]\cos(\alpha_{hkl}qx) = \tag{5.21}$$

$$\frac{1}{4}\int_{-\infty}^{\infty} dx\exp\left[\frac{-x^2}{2\sigma^2}\right]\exp[i\alpha_{hkl}qx] + \frac{1}{4}\int_{-\infty}^{\infty} dx\exp\left[\frac{-x^2}{2\sigma^2}\right]\exp[-i\alpha_{hkl}qx] \tag{5.22}$$

the latter two integrals are identical and:

$$\frac{1}{2}\int_{-\infty}^{\infty} dx\exp\left[\frac{-x^2}{2\sigma^2}\right]\cos(\alpha_{hkl}qx) = \frac{1}{2}\int_{-\infty}^{\infty} dx\exp\left[\frac{-x^2}{2\sigma^2}\right]\exp[i\alpha_{hkl}qx] \tag{5.23}$$

which is a Fourier transform of the Gaussian distribution

$$\frac{1}{2}\int_{-\infty}^{\infty} dx\exp\left[\frac{-x^2}{2\sigma^2}\right]\exp[i\alpha_{hkl}qx] = \frac{\sigma\sqrt{2\pi}}{2}\exp\left[-\frac{1}{2}\sigma^2\alpha_{hkl}^2q^2\right] \tag{5.24}$$

which after insertion into (5.20) gives:

$$A(\mathrm{q},\rho(\xi),\sigma) = C_2 = F^S\left[\int_{-\infty}^{\infty} d\xi\,\rho(\xi)\ \cos(q\ \alpha_{hkl}\ \xi)\right]\exp\left[-\frac{1}{2}(q\ \alpha_{hk\xi}\ \sigma)^2\right] \tag{5.25}$$

and since $\int_{-\infty}^{\infty} dx\cos(x) = 2\int_0^\infty dx\cos(x)$,

$$A(\mathrm{q},\rho(\xi),\sigma) = F^S\left[2\int_0^{\infty} d\xi\,\rho(\xi)\ \cos(q\ \alpha_{hkl}\ \xi)\right]\exp\left[-\frac{1}{2}(q\ \alpha_{hkl}\ \sigma)^2\right] \tag{5.26}$$

which exactly of the same form as Eqn(2.27).

References

[1] V. Luzzati, P. A. Spegt, Nature **215**, 701 (1967)

[2] Luzzati V., Tardieu A. and Gulik-Krzywicki T., *Nature* **217**, 1028-1030 (1968)

[3] Luzzati V., Gulik-Krzywicki T., and Tardieu A., *Nature* **218**, 103-106 (1968)

[4] Luzzati V., Tardieu A., Gulik-Krzywicki T., Rivas E., Reiss-Husson F., *Nature* **220**, 485-488 (1968)

[5] Scriven L. E., Nature **263**, 123 (1976)

[6] P. Barois, D. Eidam, S. T. Hyde, Journal de Physique C7 p 25 (1990)

[7] P. Strom, D. M. Anderson, Langmuir **8**, 691 (1991)

[8] P. J. Maddaford, C. Toprakcioglu, Langmuir **9**, 2368 (1993)

[9] M. H. Ropers, M. J. Stebe, V. Schmitt, J. Phys. Chem. B **103**, 3468 (1999)

[10] M. B. Sjobom, H. Edlund, B. Lindstrom, Langmuir **15**, 2654 (1999)

[11] E. L. Thomas, D. B. Alward, D. J. Kinning, D. C. Martin, D. L. Handlin, L. J. Fetters, Macromolecules **19**, 2197 (1986)

[12] D. A. Hajduk, P. E. Harper, S. M. Gruner, C. C. Honeker, E. L. Thomas, L. J. Fetters, Macromolecules 28, 2570 (1995)

[13] Nitsche J.C.C., *Lectures on Minimal Surfaces* vol 1. Cambridge University Press (1989)

[14] Hoffman D., *Nature* **384**, 28-29 (1996)

[15] A. H. Schoen, *Infinite Periodic Minimal Surfaces Without Self-intersections*, NASA Technical Note No. D-5541, Washington, DC: U.S. GPO (1970)

[16] Charvolin J. and Sadoc J.F. *J. de Physique* **48**, 1559-1569 (1987)

[17] Davis M.E. *Nature* **364**, 391-393 (1993)

[18] Anderson D.M., and Ström P. *Physica A* **178**, 151-167 (1991)

[19] De Kruijff B. *Nature* **386**, 129-130 (1997)

[20] Terrones H. and Mackay A.L. *Chem.Phys.Lett.* **207**, 45-50 (1993)

[21] Hyde S.T. and O'Keeffe M. *Phil.Trans.R.Soc.Lond. A* **354**, 1999-2008 (1996)

[22] von Schnering H.G. and Nesper R. *Angew. Chemie* **26**, 1059-1200 (1987)

[23] Klinowski J., Mackay A.L. and Terrones H. *Phil. Trans. R. Soc. Lond. A* **354**, 1975-1987 (1996)

[24] Mackay A.L. and Klinowski J. *Comp. and Math. with Appls.* (1986)

[25] Mackay A.L. *Proc. R.Soc.Lond. A* **442**, 47-59 (1993)

[26] Mackay A.L. *Chem.Phys.Lett.* **221**, 317-321 (1994)

[27] Mackay A.L. *Current Science* **69**, 151-161 (1995)

[28] von Schnering H.G. and Nesper R. *Z.Phys. B* **83**, 407-412 (1991)

[29] von Schnering H.G. and Nesper R. *Angew. Chemie* **26**, 1059-1200 (1987)

[30] Mackay A.L. *Angew. Chem. Int. Edn Engl.* **27**, 849-850 (1988)

[31] Anderson D.M. *J. de Physique, Colloq. France* **51 C7**, 1-18 (1990)

[32] Góźdź W. and Hołyst R. *J. Chem. Phys.* **106**, 9305-9312 (1997)

[33] Terrones H. *J. de Physique, Colloq. France* (1990)

[34] Góźdź W. and Hołyst R. *Phys. Rev. Lett.* **76**, 2726-2729 (1996)

[35] Góźdź W. and Hołyst R. *Phys. Rev. E* **54**, 5012-5026 (1996)

[36] Lawson B.H. *Annals of Math.* **92**, 335-374 (1970)

[37] Anderson D.M., Davis H.T., Scriven L.E. and Nitsche J.C.C. (1990), *Adv. Chem. Phys. LXXVII* **177**, 337-396 (1970)

[38] Harper P.E., Gruner S.M., *Eur. Phys. J. E*, **2**, 217-228 (2000)

[39] Harper P.E., Gruner S.M., Lewis R.N.A.H., McElhaney R.N., *Eur. Phys. J. E*, **2**, 229-245 (2000)

[40] Schwartz U.S., Gompper G., *Phys. Rev. E*, **59**, 5528-5541 (1999)

[41] Lambert, C.A, Radzilowski, R.H., and Thomas L.E. *Phil. Trans. R. Soc. Lond. A* **354**, 2009-2023 (1996)

[42] Israelachvili J.N. *Intermolecular and surface forces*, Academic Press (1985)

[43] McBain J.W., Burnett A.J. *J. Chem. Soc.* **121**, 1320-1333 (1922)

[44] Laughlin R.G. *The aqueous phase behavior of surfactants*, Colloid Science, Academic Press London (1994)

[45] Clerc M., Levelut A.M., Sadoc J.F., *Journal de Physique C7* p 97 (1990)

[46] Szleifer I. *Statistical thermodynamics of amphiphilic aggregates*, PhD dissertation, Hebrew University (1988)

[47] Takaoka Y., Pasenkiewicz-Gierula M., Miyagawa H., Kitamura K., Tamura Y., Kusumi A., *Biophysical Journal* **79**, 3118-3138 (2000)

[48] Larsson K., Fontell K., *Chem. Phys. Lipids* **27**, 321-328 (1980)

[49] Lindblom G. Larsson K. Johansson L. Fontell K. Forsen S.J. *Am. Chem. Soc.* **101**, 5465-5470 (1969)

[50] Longley W., McIntosh T.J., Nature **303**, 612-614 (1983)

[51] A. L. Mackay, Nature **314**, 604 (1985)

[52] Turner D.C., Wang Z.G., Gruner S.M., Mannock D.A., McElhaney R.N., *J. Phys. II France* **2**, 2039-2063 (1992)

[53] Landh, T. *J.Phys. Chem.* **98**, 8453-8462 (1994)

[54] Kresge, C.T., Leonowicz, M.E., Rothe, W.J., Vartuli, J.C., and Beck, J.S. *Nature* **359**, 710-712 (1992)

[55] M. Clerc, E. Dubois-Violette, *J. Phys. II France* **4**, 275 (1994)

[56] Garstecki P., Hołyst R., *J. Chem. Phys.*,**113**, 3772-3779 (2000)

[57] Velev O.D., Gurkov T.D., Ivanov I.B., and Borwanka R.P., *Phys. Rev. Lett.* **75**, 264-267 (1995)

[58] Shi A., *J. Phys: Condens. Matt.* **11**, 10183-10197 (1999)

[59] Cullity B.D., *Elements of X-ray diffraction*, Addison-Wesley Pub. Comp. (1956)

[60] Teubner M., and Strey R., *J.Chem.Phys. 87*, 3195-3200 (1987)

[61] Keller S.L., Gruner S.M., Gawrisch K. *Biochimica et Biophysica Acta* **1278**, 241-246 (1996)

[62] Wang X., Quinn P.J., *Biophysical Chemistry* 80, 93-101 (1999)

[63] Angelova A., Ionov R., Koch M.H.J., Rapp G.,*Arch. Biochem. Biophys.* **378**, 93-106 (1999)

[64] Darkes M.J.M., Davies M.A., Bradshaw J.P.,*FEBS Letters*, **461**, 178-182 (1999)

[65] Erbes J., Czeslik C., Hahn W., Winter R., Rappolt M., Rapp G., *Ber. Bunsenges. Phys. Chem.* 98, 1287-1292 (1994)

[66] Li X., Kunieda H.,*Langmuir* **16**, 10092-10100 (2000)

[67] Gustafsson J., Ljusberg-Wahren H., Almgren M., Larsson K., *Langmuir* **13**, 6964-6971 (1997)

[68] Lee Y.S., Surjadi D., Rathman J.F.,*Langmuir* **16**, 195-202 (2000)